

The Colorado State University Convective CLOUD Outflows and UpDrafts Experiment (C³LOUD-Ex)

Susan C. van den Heever, Leah D. Grant, Sean W. Freeman,
Peter J. Marinescu, Julie Barnum, Jennie Bukowski, Eleanor Casas,
Aryeh J. Drager, Brody Fuchs, Gregory R. Herman, Stacey M. Hitchcock,
Patrick C. Kennedy, Erik R. Nielsen, J. Minnie Park, Kristen Rasmussen,
Muhammad Naufal Razin, Ryan Riesenberg, Emily Riley Dellaripa,
Christopher J. Slocum, Benjamin A. Toms, and Adrian van den Heever

ABSTRACT: The intensity of deep convective storms is driven in part by the strength of their updrafts and cold pools. In spite of the importance of these storm features, they can be poorly represented within numerical models. This has been attributed to model parameterizations, grid resolution, and the lack of appropriate observations with which to evaluate such simulations. The overarching goal of the Colorado State University Convective CLOUD Outflows and UpDrafts Experiment (C³LOUD-Ex) was to enhance our understanding of deep convective storm processes and their representation within numerical models. To address this goal, a field campaign was conducted during July 2016 and May–June 2017 over northeastern Colorado, southeastern Wyoming, and southwestern Nebraska. Pivotal to the experiment was a novel “Flying Curtain” strategy designed around simultaneously employing a fleet of uncrewed aerial systems (UAS; or drones), high-frequency radiosonde launches, and surface observations to obtain detailed measurements of the spatial and temporal heterogeneities of cold pools. Updraft velocities were observed using targeted radiosondes and radars. Extensive datasets were successfully collected for 16 cold pool–focused and seven updraft-focused case studies. The updraft characteristics for all seven supercell updraft cases are compared and provide a useful database for model evaluation. An overview of the 16 cold pools’ characteristics is presented, and an in-depth analysis of one of the cold pool cases suggests that spatial variations in cold pool properties occur on spatial scales from $O(100)$ m through to $O(1)$ km. Processes responsible for the cold pool observations are explored and support recent high-resolution modeling results.

KEYWORDS: Cold pools; Updrafts/downdrafts; Convective storms; In situ atmospheric observations; Radars/Radar observations; Radiosonde/rawinsonde observations; Surface observations

<https://doi.org/10.1175/BAMS-D-19-0013.1>

Corresponding author: Susan C. van den Heever, sue.vandenheever@colostate.edu

In final form 10 March 2021

©2021 American Meteorological Society

For information regarding reuse of this content and general copyright information, consult the [AMS Copyright Policy](#).

AFFILIATIONS: S. van den Heever, Grant, Freeman, Bukowski, Casas, Kennedy, Rasmussen, Razin, Riesenber**g**, Riley Dellari**pa**, and Toms—Department of Atmospheric Science, Colorado State University, Fort Collins, Colorado; Marin**escu**—Cooperative Institute for Research in the Atmosphere, Colorado State University, Fort Collins, Colorado; Barn**um**—Laboratory for Atmospheric and Space Physics, University of Colorado Boulder, Boulder, Colorado; Dr**ager**—Department of Earth and Atmospheric Sciences, University of Nebraska–Lincoln, Lincoln, Nebraska; F**uchs**—WeatherFlow, Fort Collins, Colorado; Her**man**—Amazon.com, Seattle, Washington; Hit**chcock**—ARC Centre of Excellence for Climate Extremes and School of Earth Sciences, University of Melbourne, Melbourne, Australia; Ni**elsen**—Department of Atmospheric Sciences, Texas A&M University, College Station, Texas; Pa**rk**—Brookhaven National Laboratory, Upton, New York; Slo**cum**—NOAA/NESDIS/Center for Satellite Applications and Research, Fort Collins, Colorado; A. van den Heever—Green Energy Options Limited, Cambridge, United Kingdom

Deep convective storms assume a wide range of morphologies and are found in continental and maritime regions throughout the tropics and midlatitudes. They play a fundamental role in producing freshwater (e.g., Nesbitt et al. 2006); vertically distributing energy, water, and trace gases (e.g., Mullendore et al. 2005); cloud radiative forcing (e.g., Hartmann 2016); driving the large-scale circulation (e.g., Riehl and Malkus 1958); initiating new convection (e.g., Weckwerth et al. 2008); and generating severe weather (e.g., Zipser et al. 2006). As such, deep convective storms both support and threaten life on Earth, and the need to better understand and predict these storms is becoming increasingly critical with growing world populations and changing climates. However, accurately predicting such storms remains challenging, a fact recently highlighted by several international and national scientific bodies. The World Climate Research Programme (WCRP) is focusing specifically on storms, heavy precipitation, heat waves, and droughts as part of their “Understanding and Predicting Weather and Climate Extremes Grand Challenge” (Zhang et al. 2013), and the National Academies of Sciences, Engineering and Medicine have highlighted the need to understand the frequency, occurrence, and heavy precipitation produced by convective storms as one of the most important priorities in the 2017–27 Decadal Survey (NASEM 2018).

It has long been recognized that deep convective storms are composed of a number of intricately linked features including updrafts and cold pools (Byers and Braham 1949; Doswell 2001; Grant and van den Heever 2014; Marion and Trapp 2019). Convective updrafts are driven by latent heating, buoyancy, and vertical pressure gradients, and their velocities range from 5–10 m s⁻¹ in tropical maritime convection (LeMone and Zipser 1980; Zipser and Lemone 1980) to 50–70 m s⁻¹ in midlatitude supercells (Browning 1965; Musil et al. 1986; DiGangi et al. 2016; Lehmiller et al. 2001). Cold pools, on the other hand, are formed through latent cooling due to evaporation and/or melting and are a surface manifestation of storm downdrafts. They range in depth from 100–200 m (Gaynor and Mandics 1978) to nearly 5 km (Bryan et al. 2005; Bryan and Parker 2010), in horizontal extent from a few kilometers (Feng et al. 2015) to hundreds of kilometers (e.g., Johnson and Hamilton 1988), and have mean temperature deficits from as little as 1 K to more than 11 K (Engerer et al. 2008). The interactions of updrafts and cold pools can play a pivotal role in determining convective storm characteristics. New convective updrafts can be initiated by cold pools and cold pool collisions (Purdom 1976, 1982; Simpson et al. 1980; Droegemeier and Wilhelmson 1985; Weckwerth and Wakimoto 1992; Tompkins 2001). Cold pools also impact the orientation of the updraft (Thorpe et al. 1982; Rotunno et al. 1988), the concentration of near-surface rotation (Brooks et al. 1994; van den Heever and Cotton 2004; Snook and Xue 2008; Houston 2016), and convective organization (Weckwerth and Wakimoto 1992; Jeevanjee and Romps 2013; Grant et al. 2020), all of which feed back to updraft intensity and longevity. The strength of the cold pool is fundamental to determining the rate at which it travels (Benjamin 1968), and hence its ability to

impact storm intensity and longevity through its location relative to the parent storm updraft (Wilhelmson and Chen 1982; Droegemeier and Wilhelmson 1985). The cold pool strength, in turn, is impacted by the microphysical processes (van den Heever and Cotton 2004; Dawson et al. 2010) and organization (Houston and Wilhelmson 2011) of the parent storm which, in turn, are a function of the storm updraft.

Accurately simulating convective storms remains a challenging problem for numerous reasons. First, insufficient grid resolution has been found to impact the structure and velocities of simulated storm updrafts, with model grid spacings of 100–250 m having been found necessary for numerical solutions to converge (Bryan et al. 2003; Lebo and Morrison 2015; Jeevanjee 2017). Model grid spacing also impacts cold pool generation, propagation, frequency, and intensity, and horizontal grid spacings of $O(100)$ m are necessary to correctly represent cold pool processes (Droegemeier and Wilhelmson 1987; Straka et al. 1993; Bryan et al. 2003; Grant and van den Heever 2016; Hirt et al. 2020). Second, while convective updrafts are impacted by temperature, moisture, and wind shear (Weisman and Klemp 1982), much is still not understood about environmental controls on storms (Zipser et al. 2006; McCaul and Cohen 2002; Grant and van den Heever 2015) and the impacts of storms on their environments (Trapp et al. 2016). Furthermore, the differences between environments producing severe and more benign weather are often subtle and difficult to predict (Markowski and Richardson 2009; Coffey et al. 2017). Environmental factors, including relative humidity, temperature, wind shear, and static stability, also fundamentally impact cold pool strength and propagation speeds (Xue et al. 1997; Liu and Moncrieff 2000; Seigel and van den Heever 2012; Zuidema et al. 2017; Marion and Trapp 2019). Third, the parameterization of microphysical processes has been shown to significantly impact simulated cold pools (van den Heever and Cotton 2004; Dawson et al. 2010; Morrison et al. 2012), and several recent studies have attributed the differences between simulated and Doppler-estimated updraft velocities to the nonlinear feedbacks between the dynamics and the ice-phase microphysics parameterizations (Varble et al. 2014; Marinescu et al. 2016; Fan et al. 2017), though these differences could also be due to uncertainties in dual-Doppler estimates of updraft velocities. Finally, a number of studies have demonstrated the impacts of land surface parameterizations on modeled cold pool processes, and have highlighted the need for including a fully interactive land surface parameterization (Gentine et al. 2016; Grant and van den Heever 2016, 2018; Drager and van den Heever 2017; Fast et al. 2019; Drager et al. 2020).

If we are to improve our representation of updraft and cold pool processes within high-resolution numerical models, we need high-resolution spatial and temporal observational datasets collected under a wide range of environmental conditions. While past field campaigns have successfully used radars to measure deep convective updrafts (Davis et al. 2004; Weisman et al. 2015; Jensen et al. 2016), analysis methods (Nelson and Brown 1987; Miller and Fredrick 1998; Collis et al. 2010) and sensitivities to the spatial and temporal resolution of the data (Bousquet et al. 2008; Potvin et al. 2012) produce Doppler estimate uncertainties that are difficult to characterize (Oue et al. 2019). On the other hand, in situ radiosonde estimates of updraft velocities based on GPS-derived radiosonde ascent rates are impacted by balloon buoyancy, balloon icing, and environmental turbulence (Davies-Jones and Henderson 1975; Wang et al. 2009; Marinescu et al. 2020). Additional observations of the same convective updrafts obtained using different observational platforms under a variety of environmental conditions are therefore still necessary, both to reduce some of these velocity estimate uncertainties and to evaluate simulated storms.

Cold pool processes have been successfully investigated through the use of instrumented towers (Charba 1974; Goff 1976), the Oklahoma (Engerer et al. 2008) and mobile mesonets (Markowski et al. 2002), radiosondes and radar (Wakimoto 1982; Bryan and Parker 2010;

Hitchcock et al. 2019; Borque et al. 2020), Doppler lidars (Soderholm et al. 2016), and drones (Houston et al. 2012; Riganti and Houston 2017). While these studies have provided useful information on cold pool processes and variability, the number of cold pools observed has been limited, the information was not obtained above the surface, the spatial resolution of observations was too coarse, or the observations were not obtained parallel to the gust front to allow for the three-dimensional evaluation of cold pool processes simulated using high-resolution models. More specifically, these studies cannot be used to assess cold pool processes and the heterogeneity of cold pool characteristics on scales from $O(100)$ m through $O(1)$ km in a three-dimensional framework (parallel to the gust front, perpendicular to the gust front, and in the vertical).

The overarching goal of the Colorado State University Convective CLOUD Outflows and UpDrafts Experiment (C³LOUD-Ex) was to enhance our understanding of deep convective storm processes, in particular updrafts and cold pool processes, and improve their representation within high-resolution numerical models. To achieve this goal, C³LOUD-Ex had three specific objectives:

- 1) to obtain high spatial [from $O(100)$ m through $O(1)$ km] and temporal (seconds) resolution measurements of cold pool and gust front characteristics, at and above the surface, both parallel and perpendicular to gust front;
- 2) to obtain observations of updraft velocities using multiple radar and radiosonde platforms; and
- 3) to evaluate and enhance the representation of updraft and cold pool processes through model-observation comparisons of high-resolution C³LOUD-Ex case study simulations.

Pivotal to C³LOUD-Ex was a novel observational strategy designed around simultaneously employing a fleet of drones [also known as small uncrewed aerial systems (sUAS) or uncrewed aerial vehicles (UAV)], high-frequency radiosonde launches, and surface observations, referred to as the “Flying Curtain,” to obtain simultaneous measurements of the spatial and temporal heterogeneities of cold pools parallel and perpendicular to the cold pool boundary. Convective updraft observations were obtained through the combined use of updraft-targeted radiosondes and weather radars.

The primary purpose of this paper is to describe the instruments and measurement strategy used in the field campaign, present an overview of the observations made for each of the field campaign days, and discuss the bulk characteristics of the storm systems that were observed. Preliminary analysis of a cold pool case study will also be presented.

Field campaign and instrumentation description

Campaign location and duration. The C³LOUD-Ex field campaign was conducted during 11–20 July 2016 and 1 May–12 June 2017 over northeastern Colorado, southeastern Wyoming, and southwestern Nebraska (Fig. 1). This region was selected as isolated deep convective storm systems are frequently observed here during the spring and early summer (Cotton et al. 2010). A wide variety of convective storm types and associated cold pool features were observed during the campaign (Fig. 2; Table 1), including single cell thunderstorms, multicellular storms, and supercells, the latter of which ranged from weaker left-moving low precipitation supercells (Fig. 2a) (Davies-Jones et al. 1976; Bluestein and Parks 1983) through to strong right moving classic supercells (Browning 1965; Doswell and Burgess 1993) that produced weak tornadic circulations at the surface (Fig. 2d). Sixteen cold pool case studies produced by various storm morphologies, and seven supercell updraft case studies, were successfully obtained during C³LOUD-Ex. The dates of each of the case studies, as well as a basic description of the storm characteristics and the types of observations made, are shown in Table 1.

Drones. To measure heterogeneities in cold pool temperature, pressure and moisture simultaneously at and above the surface, both parallel and perpendicular to the gust front, a total of seven different multirotor drones were employed. Six of the drones used in C³LOUD-Ex were DJI Matrice 600 Pros, and the other was a DJI Matrice 600. The six Matrice 600 Pro hexacopter drones (DJI 2017) (Fig. 3e) served as the primary platforms for our operations in 2017, while the Matrice 600 drone (DJI 2016) was the primary drone used in 2016. While Federal Aviation Administration (FAA) regulations typically restricts drone flights to 400 ft (~122 m) AGL, a waiver to allow flights to 1,200 ft (~366 m) AGL for a subset of the C³LOUD-Ex area (Fig. 1) was granted by the FAA (waiver number 107W-2017-00889). This waiver was the third Part 107 altitude waiver ever granted and the largest granted at the time (FAA 2017). While the waiver extended the altitudes sampled by the drones, it should be noted that sampling the full vertical extent of cold pools with the drones was not always possible as some cold pools had depths of several kilometers. Measurements of the full extent of the cold pools were, however, obtained using the radiosondes (as discussed in the next section).

Each drone carried a DJI Zenmuse X3 camera and an

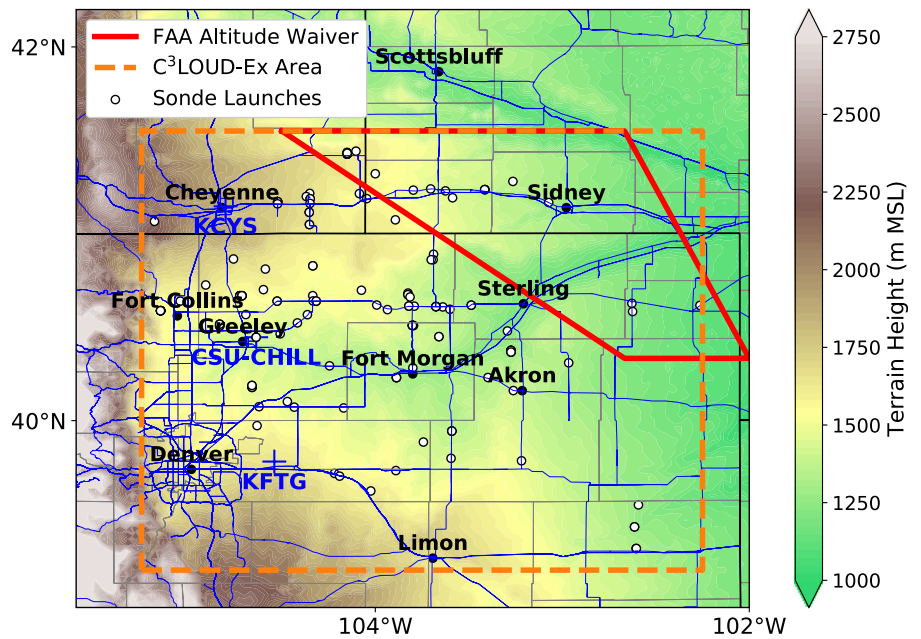


Fig. 1. The specific locations of the C³LOUD-Ex field campaign conducted within Colorado, Wyoming, and Nebraska. The shading demonstrates the topography of the region, the dashed orange line represents the field campaign region, the red line outlines the area in which the FAA drone waiver was applicable, the blue crosses show the location of the Denver (KFTG) and Cheyenne (KCYS) NEXRAD radars and the CSU-CHILL radar, the white dots represent the locations of the radiosonde launches, and the black dots indicate cities and towns within the region.

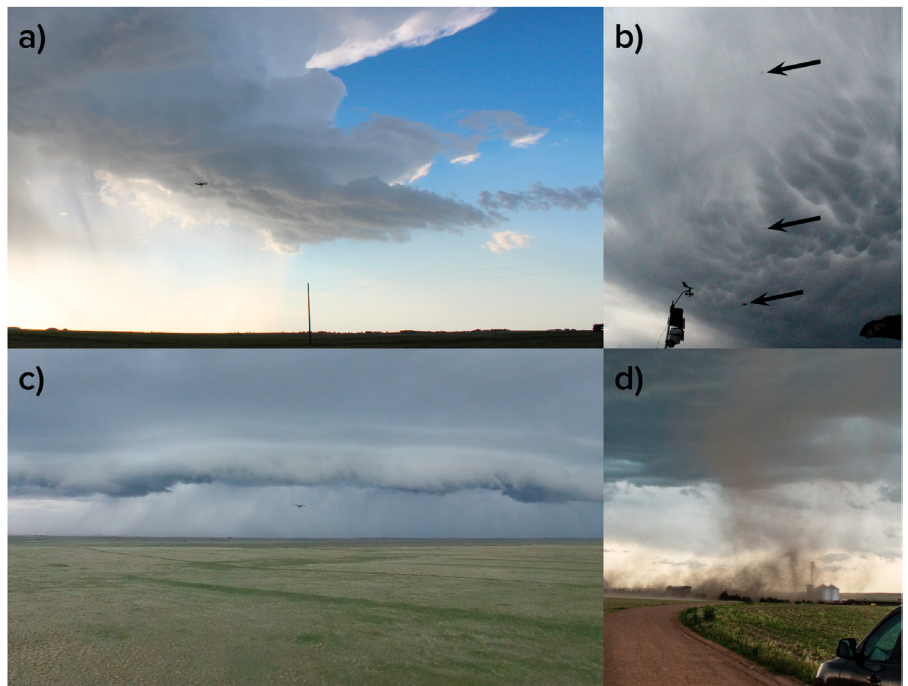


Fig. 2. Some of the storm types and storm features observed during C³LOUD-Ex. (a) A counterclockwise rotating left moving supercell (8 Jun 2017); (b) one of the towers of three vertically stacked drones (indicated by the black arrows) within the deep deployment located under a convective anvil (5 Jun 2017); (c) a strong outflow boundary under a precipitating anvil (25 May 2017); and (d) weak rotation on the ground in association with the supercell observed on 25 May 2017.

Table 1. The cold pool and updraft case studies successfully sampled during C³LOUD-Ex.

Date	Basic description	Surface	Drones	Soundings	CHILL	Disdrometer
Cold pools						
17 Jul 2016	Long-lived (~5 h) supercell in southeast WY and northeast CO	3	1	11	Yes	No
18 Jul 2016	Cold pool from thunderstorm with high lightning frequency	2	2	6	Yes	No
2 May 2017	Weak, rainy cold pool in north central CO	3	6	5	Yes	No
7 May 2017	Severe-warned cold pool in north central CO	3	6	2	Yes	No
13 May 2017	Late evening cold pool sampling	3	5	7	No	No
17 May 2017	Clear sky sampling of isolated cold pool	3	6	9	Yes	No
25 May 2017	Strong cold pool under precipitating anvil	2	2	6	Yes	Yes
26 May 2017	Measurements of supercell cold pool	3	4	12	Yes	No
31 May 2017	Southward propagating, enormous supercell	2	6	10	Yes	No
1 Jun 2017	Weak, tropical-like cold pools	3	5	6	Yes	Yes
5 Jun 2017	Two separate cold pools: 1) first deep drone deployment and 2) a weak westward-propagating cold pool	2	6	9	Yes	Yes
6 Jun 2017	Weak cold pool near CSU-CHILL radar in which the radiosondes were evident on scans	3	6	7	Yes	Yes but not collocated
7 Jun 2017	Two separate cold pools: 1) second deep drone deployment and 2) a strong westward-moving cold pool	2	4	11	Yes	No
8 Jun 2017	Third deep drone deployment through cold pool associated with left-moving supercell	3	6	9	Yes	Yes
Updrafts						
17 Jul 2016	Long-lived (~5 h) supercell in southeast WY and northeast CO	3	1	11	Yes	No
16 May 2017	Long-lived (~6 h), strong supercell in far eastern CO	1	0	5	Yes	No
25 May 2017	Weak tornadoes observed on the ground	2	2	6	Yes	Yes
26 May 2017	Isolated, long-lived (~6 h) supercell; multiple tornadoes reported; circulation seen on the ground	3	4	12	Yes	No
31 May 2017	Southward propagating, enormous supercell that interacted with various boundaries	2	6	10	Yes	No
7 Jun 2017	Many scattered, intense supercells	2	4	11	Yes	No
12 Jun 2017	Low-precipitation supercell near foothills of Fort Collins	0	0	2	Yes	Yes

iMet-XQ pressure, temperature, and humidity sensor manufactured by International Met Systems (Grand Rapids, MI), the specifications of which are listed in Table 2. Three Matrice 600 Pros were also outfitted with downward pointing FLIR Systems (Wilsonville, OR) Duo R dual visible and longwave infrared cameras to measure the surface temperature response to the cold pool passage. The iMet-XQ sensors were mounted immediately above the Zenmuse X3 cameras on board all seven drones. Previous studies have demonstrated the need to test the location of the sensors on various drone platforms (Greene et al. 2019; Islam et al. 2019). The sensitivity of the location of the sensors with respect to the drone propeller wash, batteries, radiation, and aspiration were therefore extensively tested, the results of which are to be published elsewhere. However, given that some preliminary cold pool analyses are presented below, the observational accuracy of the drone platforms in determining the changes in temperature and relative humidity across the gust front is demonstrated through comparisons with corresponding radiosonde observations (see the next section) in the scatterplot shown in Fig. 4. Difference measurements are shown in this figure as they are of interest in this study given our focus on comparisons between pre- and post-cold pool conditions, although this does not allow us to examine systematic biases. It is clear from Fig. 4 that the differences between the radiosonde and drone measurements of the temperature and relative humidity changes across the gust front are generally less than 1 K and

10%, respectively. As such, these demonstrate reasonable agreement between the two instruments considering the stated instrument accuracies (Table 2) and the additional uncertainties associated with radiative heating and with thermal and airflow effects introduced by the drones.

radiosondes. Portable and fully mobile balloon platforms have become a regular feature in field studies of deep convection (e.g., Rasmussen et al. 1994; Davis et al. 2004; Wurman et al. 2012; Trapp et al. 2016; Geerts et al. 2017) and are a way to collect in situ observations of both cold pools and updrafts. C³LOUD-Ex teams launched a total of 148 soundings from two minivans (Table 2; Fig. 3b). The location of each launch is shown in Fig. 1. Magnets were used to attach the radiosonde receivers to the vehicle roofs, which allowed for continued monitoring of the radiosondes while we repositioned our vehicles for the next radiosonde launch, as well as for quick detachments during inadvertent conditions such as large hail. Similar receiver mounts were used in the Mesoscale Predictability Experiment (MPEx) and were also fundamental to their mobile strategy (Trapp et al. 2016). iMet radiosondes do not require additional calibration prior to launch, which is ideal for launching sondes in quick succession to sample the rapidly evolving environments of deep convective storms and fast-moving cold pools, and the iMetOS-II software allowed for real-time data processing. To simplify updraft speed calculations, the details of which are described in Marinescu et al. (2020), operators aimed to consistently fill the 200-g balloons with the same amount of helium.

Radar. C³LOUD-Ex operations were performed primarily in the vicinity of an approximately south-to-north radar array located along the front range urban corridor of Colorado and Wyoming (Fig. 1). This includes two dual-polarization, S-band Weather Surveillance Radar-1988 Doppler (WSR-88D; NOAA 1991) located near Denver, Colorado (KFTG) and Cheyenne, Wyoming (KCYS), and the dual-polarization, dual-frequency (S and X band) Colorado State University–University of Chicago–Illinois State Water Survey (CSU-CHILL) Doppler radar

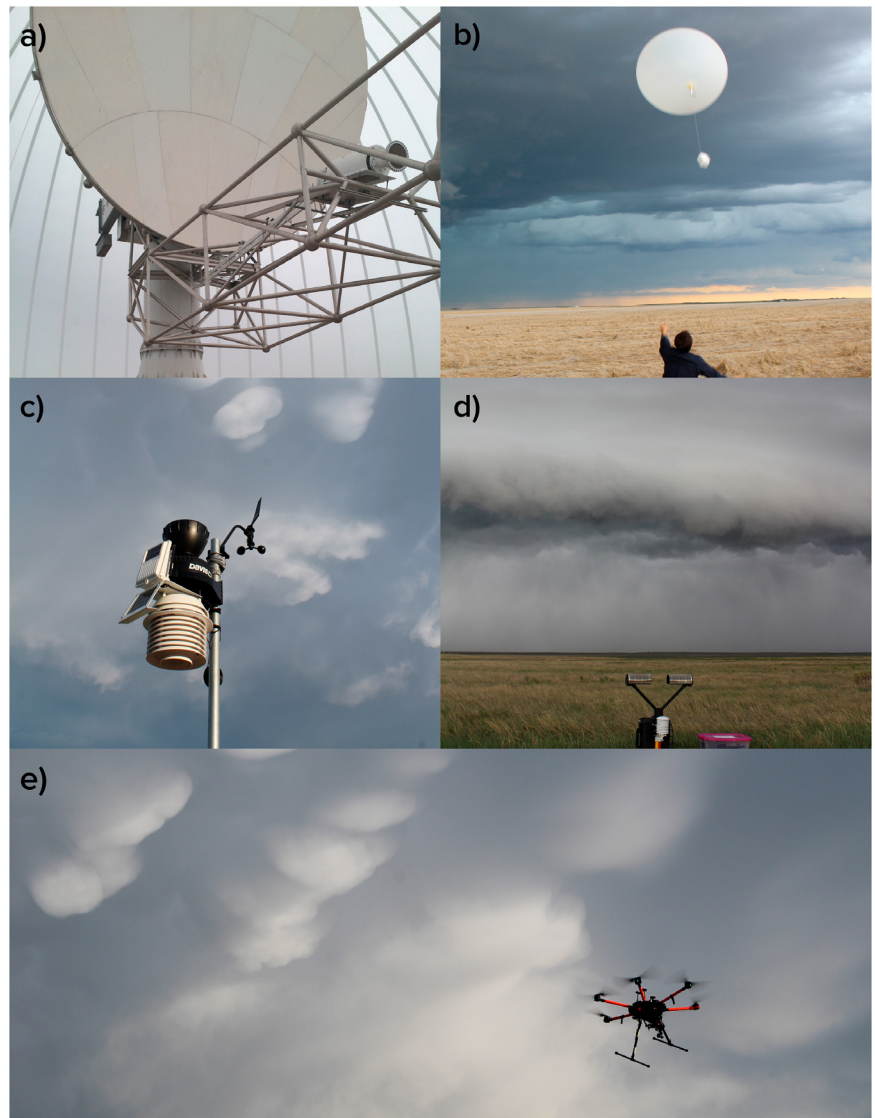


Fig. 3. Photographs of the C³LOUD-Ex instrumentation utilized in the field: (a) the CSU-CHILL radar, (b) iMet radiosondes, (c) Davis Instruments surface stations, (d) a mobile Parsivel-2 disdrometer, and (e) a Matrice 600 Pro drone in takeoff/landing configuration.

in Greeley, Colorado (Fig. 3a) (Brunkow et al. 2000; Junyent et al. 2015). While the WSR-88D scan strategies are adapted depending on the current weather, the CSU-CHILL scanning strategy was rapidly adaptable for achieving the C³LOUD-Ex objectives. Coordinating with the field operations, team members operated the CSU-CHILL radar, tailoring the scanning strategy to focus on updrafts or cold pools. A combination of multiple range-height indicator (RHI) scans and lower-troposphere, plan-position indicator (PPI) scans were employed at high temporal frequency (less than 2 min per suite of scans) to capture both the horizontal and vertical evolution of cold pools. For radar-derived estimates of in-storm vertical motion via dual-Doppler analyses, PPI scans from CSU-CHILL were closely synchronized in time with those from either KFTG or KCYS. RHI scans were also performed using CSU-CHILL to obtain observations of the vertical structures of the updrafts.

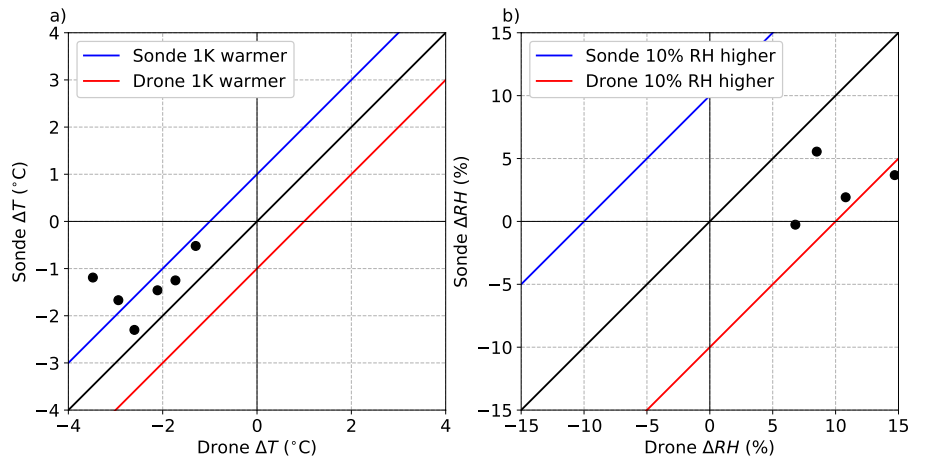


Fig. 4. (a) Scatterplot comparing the changes in temperature observed across the cold pool boundary (ΔT) between collocated radiosonde and drone measurements (black dots) in the 17 May 2017 cold pool case study described in the “C³LOUD-Ex Cold Pools” section below. The radiosonde observations closest in height and time to the drone observations were used for this comparison, where the radiosonde observations were required to be within ± 2.5 m in height of the drone observations. The black 1:1 line represents a perfect agreement between the drone and radiosonde measurements; the blue 1:1 line denotes the constant line where the radiosonde ΔT is 1 K warmer than the drone ΔT , and the red line denotes the constant line where the drone ΔT is 1 K warmer than the radiosonde ΔT . (b) As in (a), but for relative humidity (ΔRH ; %), where the blue and red lines indicate 10% departures in RH from a perfect correlation between the two. There are fewer points in (b) compared with (a) due to RH data quality issues with one of the drone RH sensors on this day.

Table 2. Specifications of the meteorological sensors using in C³LOUD-Ex.

Sensor	Type	Stated instrument accuracy (\pm)
Drones: iMet-XQ Meteorological Sensor (International Met Systems 2016)		
Temperature	Bead thermistor	0.3°C
RH	Capacitive	5%
Pressure	Piezoresistive	1.5 hPa
Radiosondes: iMet-a-ABxn Meteorological Sensor (International Met Systems 2016)		
Temperature	Bead thermistor	0.2°C
RH	Capacitive	5%
Pressure	Piezoresistive	0.5 hPa
GPS	CAM-M8	10 m horizontal, 15 m vertical
Surface Stations: Wireless Vantage Pro2 Integrated Sensor Suite (Davis Instruments 2013)		
Temperature	PN junction silicon diode	0.3°C
RH	Film capacitor element	2%
Pressure	Piezoresistive	1.0 hPa
Wind speed	Cup anemometer with solid state magnetic sensor	0.9 m s ⁻¹
Wind direction	Wind vane with potentiometer	3°

Surface stations. To observe meteorological conditions near the ground, three portable, identical surface stations were deployed (Fig. 3c). The Wireless Vantage Pro2 Integrated Sensor Suite manufactured by Davis Instruments was used to measure temperature, pressure, relative humidity, and winds (averaged over a 1-min time period) using fan aspirated sensors with accuracies specified in Table 2 (Davis Instruments 2013). These surface stations have previously been used in other studies that measured cold properties (e.g., Eastin et al. 2012). The instrumentation suite was attached to a 2 m AGL tripod stand and was secured with cinder blocks on the ground during high-wind conditions. Data were displayed in real time and stored on the data-logging console. The surface stations were used to establish the pre-cold pool surface conditions, to observe the passage of cold pools, and to provide a ground quality check for the radiosondes before release.

Disdrometer. A portable Parsivel-2 disdrometer (Fig. 3d) was deployed at fixed locations ahead of convective storm systems on several C³LOUD-Ex days. Drop size distribution data were output every 10 s, and a quality control method and particle classification algorithm were used to mitigate errors in the data following Friedrich et al. (2013). Various parameters were calculated to characterize the size distributions, including rainfall rate, liquid water content, and median volume diameter.

Field campaign setup and approach.

Cold pool measurement strategy. A novel measurement strategy, the Flying Curtain, was developed to investigate the spatial and temporal heterogeneities of cold pools at the appropriate scales, thereby addressing the first of the C³LOUD-Ex objectives. After deciding which cold pool to sample, C³LOUD-Ex teams drove ahead of the advancing gust front and set up the Flying Curtain as shown in Fig. 5. The 100M and 1KM points were located 100 m and 1 km away from the selected Anchor Point (ANCHR), respectively. The 100-m spacing between the ANCHR and 100M points was selected in order to evaluate the need for horizontal grid spacing on $O(100)$ m in capturing cold pool processes and variability (Droegemeier and Wilhelmson 1987; Straka et al. 1993; Bryan et al. 2003; Grant and van den Heever 2016). The 1-km spacing was chosen as it represents grid spacing often used when simulating convective storms in convection-allowing models. At each of the three points (ANCHR, 100M, 1KM), a surface station and two vertically stacked drones, one at 20 m and the other at 120 m AGL, were deployed. In this way, two horizontal rows of three drones separated by 100 m and 1 km in the horizontal, and 100 m in the vertical, were flown (Fig. 5a). Radiosondes were also simultaneously launched at the ANCHR and the 1KM fixed locations. This setup is referred to as the shallow deployment. Occasionally, when the storm system of interest fell within the requested FAA altitude wavier region, the deep deployment was flown in which two vertical towers of three drones located at 20, 120, and 350 m AGL were located at the ANCHR and 100M points, as shown in Figs. 5b and 2b. In the deep deployment configuration, radiosonde launches by the two teams were collocated, but launches were alternated in rapid succession.

During operations, the CSU-CHILL radar facilitated the identification of the advancing gust front and hence the appropriate location for the setup of the Flying Curtain, which was placed parallel to the gust front. The Flying Curtain was kept stationary relative to the ground, and measurements of the cold pool properties were obtained as the cold pool moved through and past the Flying Curtain, as shown in Fig. 6. As such, three-dimensional (parallel to the gust front, perpendicular to the gust front, and vertical) cold pool measurements were obtained in time while maintaining the appropriate spatial distance between instrumentation necessary to address the C³LOUD-Ex science objectives (Fig. 6). Furthermore, this approach meant that the cold pool properties could be analyzed without having to account for moving measurement platforms.

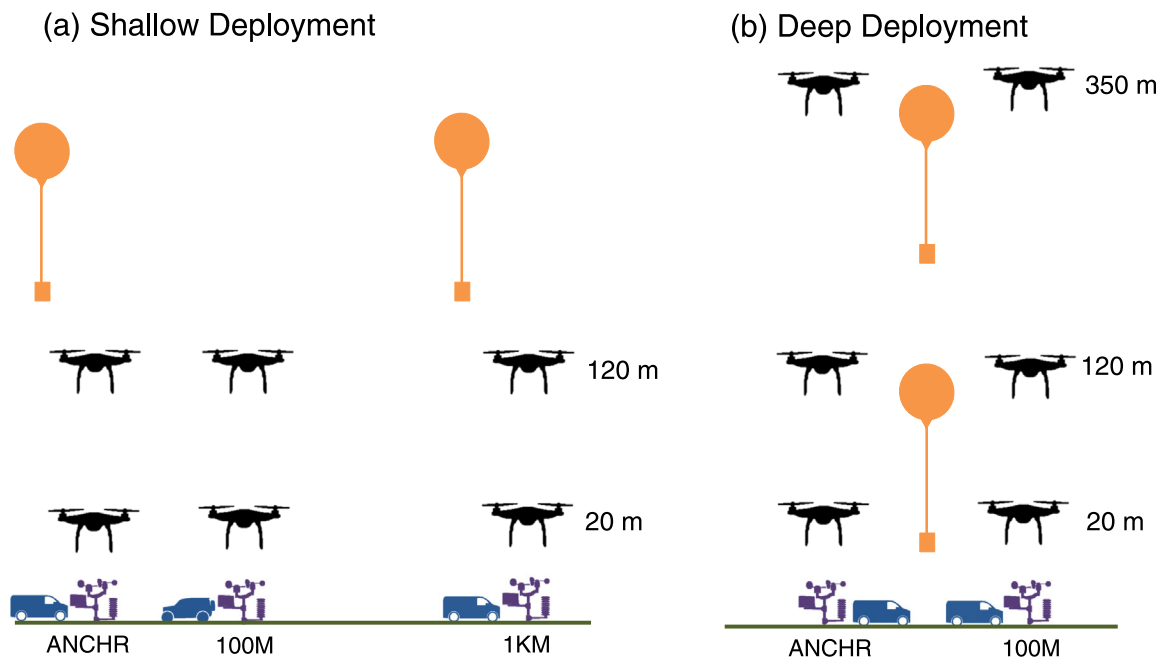


Fig. 5. The C³LOUD-Ex Flying Curtain utilized on the days focused on cold pool measurements for (a) the shallow deployment and (b) the deep deployment. The drones are indicated using black symbols, the radiosondes using orange symbols, the field campaign vehicles with blue symbols, and the surface stations with purple symbols. The 100M and 1KM points were 100 m and 1 km away from the ANCHR point in the horizontal direction.

Updraft measurement strategy. In C³LOUD-Ex, radiosondes were used to specifically target the convective updrafts, thereby observing their vertical velocities and thermodynamic characteristics, and achieving the second C³LOUD-Ex objective. While radiosondes are often employed in deep convection field campaigns, they are more typically used to obtain measurements of the storm environment as opposed to consistently measuring the updraft velocities, even though updrafts may occasionally be sampled. There have been few field efforts described in the literature that have specifically targeted updrafts using radiosondes as one of their primary goals (Davies-Jones and Henderson 1975; Bluestein et al. 1988; Rasmussen et al. 1994). Targeting the updrafts with radiosondes was challenging, and the

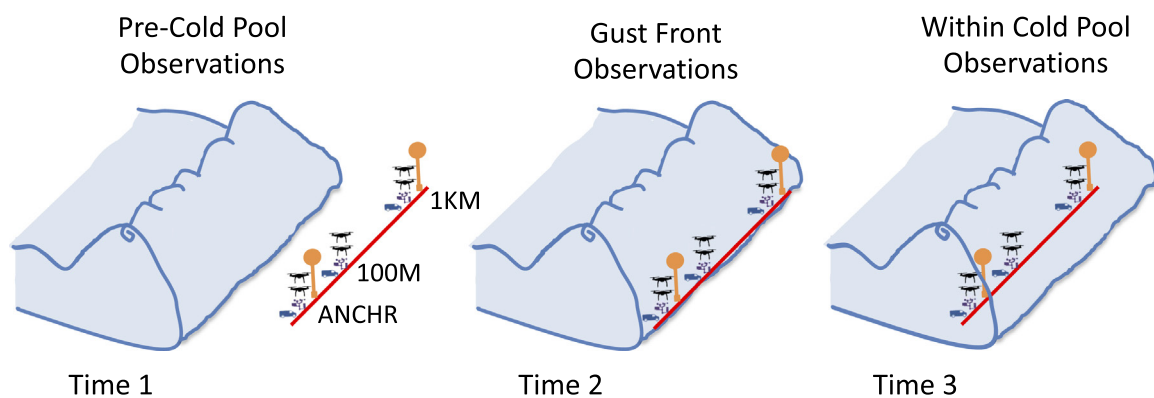


Fig. 6. The C³LOUD-Ex Flying Curtain allows for horizontal and vertical cold pool measurements to be made both parallel and perpendicular to the gust front. The cold pool is indicated by the blue shading, and the location of the Flying Curtain with the red line. The icons and observing points (ANCHR, 100M, and 1KM) are the same as those used in Fig. 5. Time 1 represents the earliest time, while Time 3 is the latest time. It is important to note that the Flying Curtain remains stationary relative to the ground, and that the cold pool moves through the Flying Curtain (from left to right in this image).

radiosondes did not always ascend directly through the primary updraft, especially due to the high cloud bases encountered during the field campaign. Various other regions of the storms were therefore also sampled. When obtaining measurements of the updraft velocities, the C³LOUD-Ex team endeavored, whenever possible, to conduct radiosonde operations within the dual-Doppler lobes, thereby facilitating the combined analysis of the in situ radiosonde data, dual-Doppler derived vertical velocities, and the PPI and RHI radar scans. Analyzing the radiosonde and radar data together, as shown in Fig. 7, and as further presented in Marinescu et al. (2020), allowed for 1) the identification of the location of the radiosonde within the storm and hence which storm features were being sampled; 2) comparisons of the in situ radiosonde GPS estimates with the dual-Doppler estimates of updraft velocities, where possible; and 3) the utilization of the dual-polarization variables to assess the microphysical conditions encountered by the balloon. The approach to determining the updraft velocities using the radiosonde GPS data, including quantifying the uncertainties in these measurements, are discussed in detail in Marinescu et al. (2020). Finally, it should be noted that while

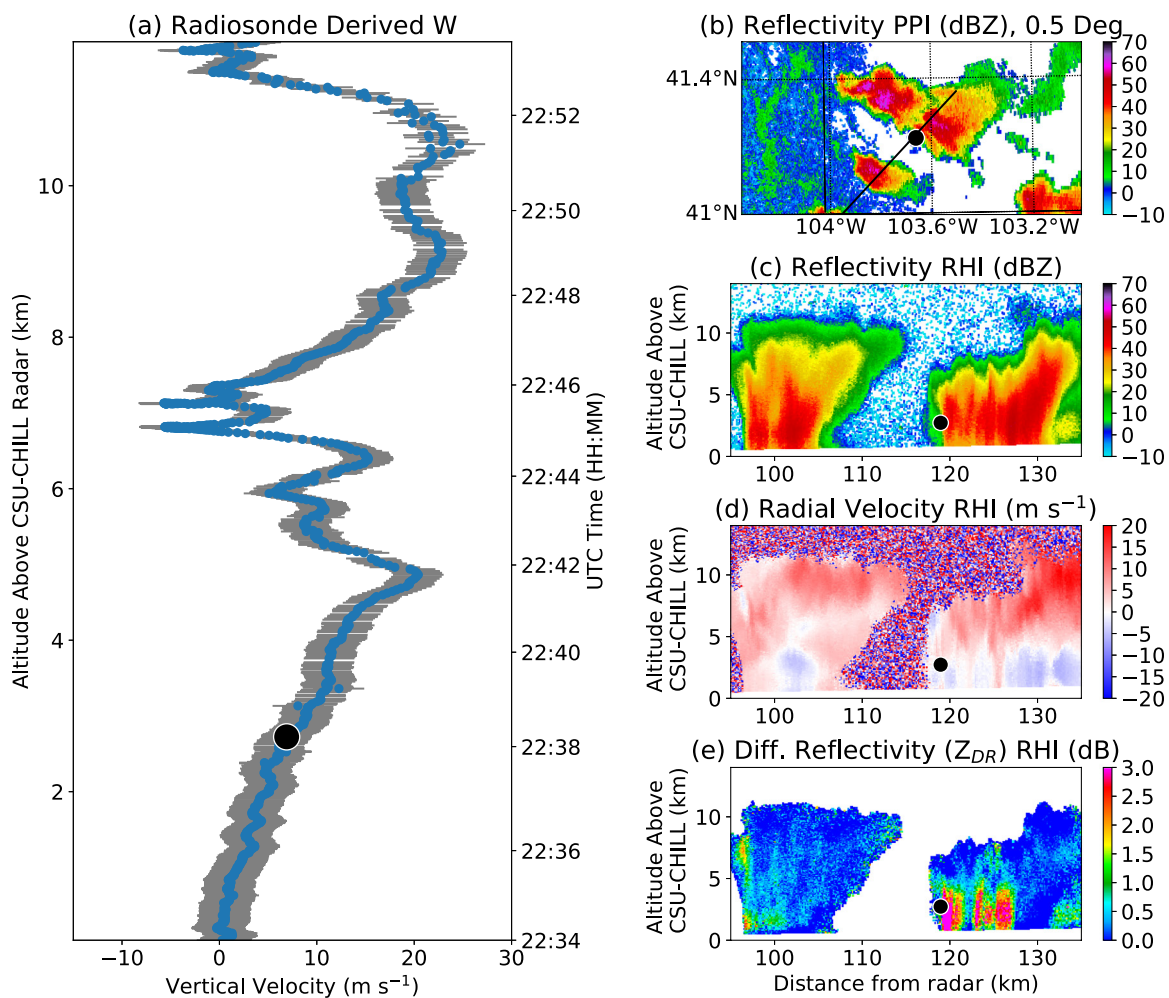


Fig. 7. (a) Vertical velocity estimates from a radiosonde launch on 7 Jun 2017, as a function of altitude and time. The vertical velocity uncertainty estimate ($\pm 2.6 \text{ m s}^{-1}$) was determined by Marinescu et al. (2020) and is indicated by the error bars on the figure. This uncertainty estimate excludes uncertainties associated with hydrometeor impacts. The black dot in (a) represents the altitude and time of one instance when a CSU-CHILL RHI scan intersected the airborne radiosonde, as shown in (b)–(e). (b) KCYS PPI scan. The black line indicates the location of the CSU-CHILL RHI scan, and the black dot shows the position of the radiosonde at the time of RHI–radiosonde intersection. CSU-CHILL RHI scans of (c) reflectivity, (d) radial velocity, and (e) differential reflectivity, respectively. The black dots in (c)–(e) also show the position of the radiosonde.

the drones were used to sample the cold pools and low-level updraft inflow air, they were not used to measure the updraft characteristics due to the FAA ceiling limits, and because it was anticipated that they would not be able to withstand the updraft velocities and turbulence encountered within deep convective storms.

Forecasting approach. Forecasting the timing of convection initiation and the intensity of convective activity was necessary to support the C³LOUD-EX field campaign activities. At long lead times, synoptic data were obtained from operationally available global models [e.g., Global Forecast System (GFS)]. The mesoscale models [e.g., North American Mesoscale (NAM)] were used at 2–3-day lead times to identify the location of moisture, instability, lift, and shear. As the terrain in the region (Fig. 1) regularly serves as an initiation point for convection (Toth and Johnson 1985; Szoke 1991; Carbone and Tuttle 2008; Lock and Houston 2015), the most critical goal at these lead times was to characterize the potential for convection to survive as it moved off the terrain. On the day of any potential deployment, the C³LOUD-Ex team relied heavily on the convection-allowing guidance from the operational and experimental High Resolution Rapid Refresh (HRRR; Benjamin et al. 2016) and NCAR Ensemble (Schwartz et al. 2015), as well as the preliminary, non-operational three-channel water vapor, split-window difference, and visible imagery from the 5-min CONUS and 1-min mesoscale sectors of *GOES-16*. The latter proved critical in tracking mesoscale boundaries, moisture convergence and convection initiation (Lindsey et al. 2014, 2018). After the initial deployment location was selected, environmental soundings were launched en route to help to assess the validity of the HRRR initialization and other model guidance, and hence aid in fine-tuning the deployment location and timing. This was important as it provided information on the strength of the capping inversion and the amount of midtropospheric moisture, both of which are often poorly resolved by the forecast models. Forecasting challenges experienced in the lee of the Rocky Mountains identified over the course of the campaign led to a study undertaking a probabilistic verification of SPC forecasts (Herman et al. 2018). Once convection initiated, forecasting shifted to nowcasting (e.g., Wilson and Mueller 1993), which focused on placing observing teams in the most favorable locations for the cold pool and updraft measurement strategies using the C³LOUD-Ex radar network and satellite imagery.

C³LOUD-Ex updrafts

In situ observations of seven supercell updrafts (Table 1) were successfully obtained using radiosondes during C³LOUD-Ex (Fig. 8), where the updraft vertical velocities were calculated using a 12-s centered-in-time derivative of the radiosonde GPS position and time measurements. The approach to estimating the updraft velocities and its uncertainties, including accounting for aspects such as balloon buoyancy, updraft turbulence, and balloon bursts, is described in detail in Marinescu et al. (2020) and are not repeated here. It is evident from Fig. 8 that there is large variability in the updraft observations, primarily due to the specific parts of the updrafts and storm systems that were sampled. In addition to the primary updrafts, features captured by these radiosonde observations include gravity wave oscillations in the cloud anvils, forward-flank downdrafts, rear-flank downdrafts, and intense upper-tropospheric downdrafts. Understanding the details of the radiosonde trajectories and the local conditions of the in situ point measurements required using the collocated radar data, as shown in Marinescu et al. (2020).

The C³LOUD-Ex supercell storm cases had surface-based CAPE values between 1,000 and 3,000 J kg⁻¹ and 0–6-km bulk wind shear of 10–30 m s⁻¹. While most of the observations were from classic supercells, the 12 June 2017 radiosonde (Fig. 8g) sampled a low-precipitation, left-moving supercell. The strongest updraft vertical velocities that were measured using the

radiosondes were recorded on 17 July 2016 (Fig. 8a), 26 May 2017 (Fig. 8d), and 12 June 2017 (Fig. 8g). This was in part because it was easier to position the mobile sounding units and launch into clearly defined updraft regions with strong inflow air on these days. In these cases, many radiosondes were successfully launched directly into the updraft core near cloud base, which is evident in the observations with continuously increasing vertical velocities (e.g., Fig. 8g), as opposed to being entrained into the updraft edges at upper levels (e.g., Fig. 8f). The maximum radiosonde updraft velocity measured throughout the field campaign was $36.2 \pm 2.6 \text{ m s}^{-1}$. However, after adjusting for instances where there is strong evidence that the radiosonde balloon burst, this maximum value increases to 49.9 m s^{-1} , which occurred on 17 July 2016 (Fig. 8a, Launch 5; estimated balloon burst and maximum updraft achieved at ~ 8.0 and $\sim 10.3 \text{ km MSL}$, respectively). The updraft velocity measurements reported here can be thought of as a lower bound on the updraft velocity estimates because of the uncertainties, such as balloon icing, that cannot be easily accounted for, and because the radiosondes frequently did not ascend through the strongest regions of the rotating updrafts.

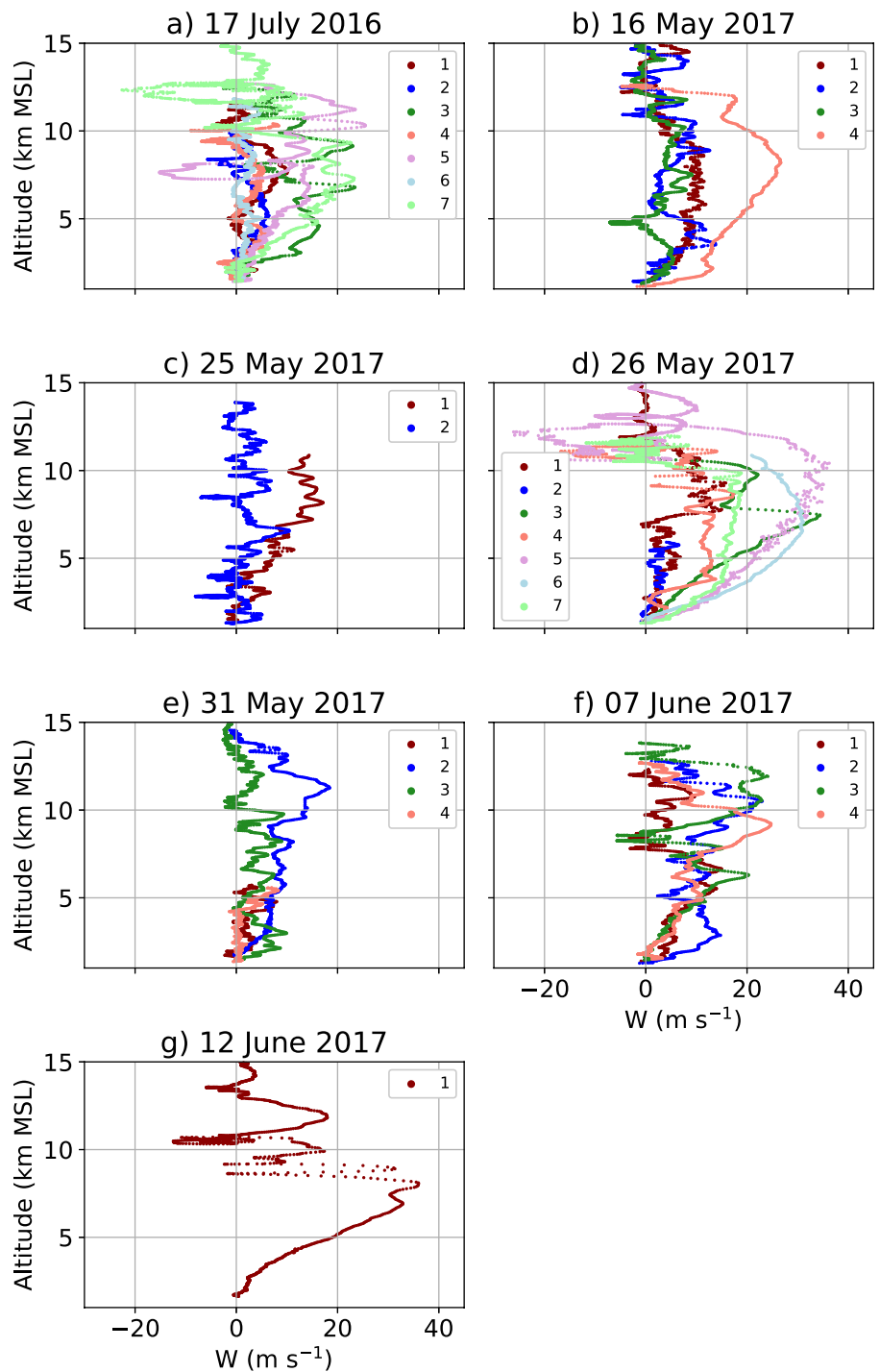


Fig. 8. (a)–(g) Estimates of the updraft vertical velocity from the updraft targeted radiosonde launches of the seven C³LOUD-Ex updraft case study days (Table 1). The different colors in each panel represent the different launches made on each day, where the lower the number the earlier the launch.

C³LOUD-Ex cold pools

Overview of the cold pool characteristics. The 16 cold pools observed during C³LOUD-Ex (Table 1) include those associated with short-lived, isolated convective cells, multicellular clusters of convection, and supercellular convection; cold pools observed under overcast skies near their parent storms (Fig. 2c) and in sunny conditions after having propagated away from

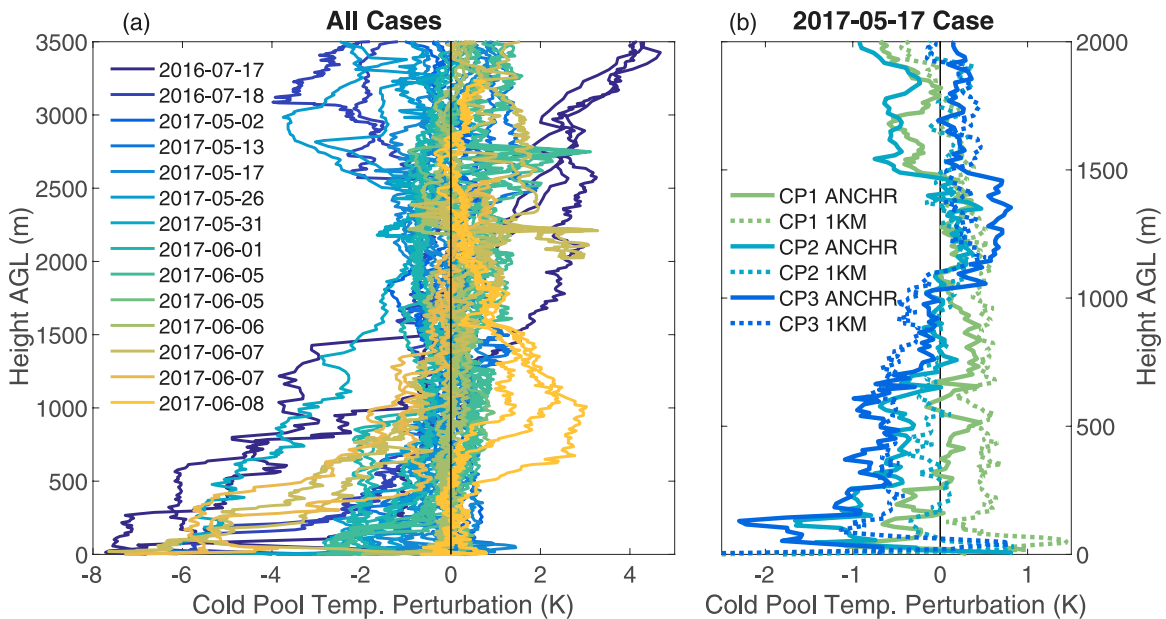


Fig. 9. (a) Temperature perturbation profiles for all of the cold pool case study soundings (Table 1) observed during the C3LOUD-Ex field campaign. Perturbations are calculated relative to the pre-cold pool sounding. (b) As in (a), but for the 17 May 2017 case only. Note that both axes in (b) are different from those shown in (a).

the parent convection; and cold pools observed as early as midday and as late as near sunset. The cold pools observed therefore have a wide range of temperature perturbations, depths, and vertical structures (Fig. 9a). Maximum temperature perturbation magnitudes (relative to the pre-cold pool soundings) range from -8 K to close to 0 K, and cold pool depths range from 200 to 2,300 m, where cold pool depth is defined simply as the lowest altitude at which the temperature perturbation ≥ 0 K, similarly to Hitchcock et al. (2019). The cold pool observed on 17 May 2017 is now analyzed in detail. The soundings specific to this case are shown in Fig. 9b to facilitate this analysis. This case study demonstrates the strength of using the combined C³LOUD-Ex datasets to 1) better understand cold pool processes, 2) assess the spatial and temporal variability of cold pool characteristics both perpendicular and parallel to the gust front, and 3) provide observational evidence to assess several hypotheses advanced in two recent cold pool modeling studies (Grant and van den Heever 2016, 2018).

Cold pool case study: 17 May 2017. The cold pool forming on this day was produced by a convective storm that developed along the Cheyenne Ridge, to the southeast of Cheyenne, Wyoming (Fig. 1). The cold pool propagated southward toward the CSU-CHILL radar (Fig. 10), where it was observed near Pierce, Colorado, under clear-sky conditions. The Flying Curtain was set up parallel to the gust front of the advancing cold pool, as indicated by the black dots in Figs. 10a and 10b. All three shallow deployment positions (ANCHR, 100M, and 1KM) (Fig. 5a) were oriented in an east–west direction, where ANCHR was the farthest west (Fig. 10). In total, data from four pairs of sounding launches, six drones, three surface stations and the CSU-CHILL radar were obtained (Table 1).

The gust front propagated through the Flying Curtain between 2000 and 2030 UTC [1400 and 1430 local time (LT)]. The gust front is clearly evident as a line of enhanced reflectivity in the CSU-CHILL PPI sector scans (Figs. 10a,c), with wind velocities to the north of the gust front reaching approximately 10 m s^{-1} (Figs. 10b,d). RHI scans through the cold pool (Figs. 10e,f) depicted a classic density current structure including a deeper head and shallower tail region, as indicated by the solid curved black line in Figs. 10e and 10f, and cold pool depths of 1–1.5 km throughout the sampling time period (Fig. 9b).

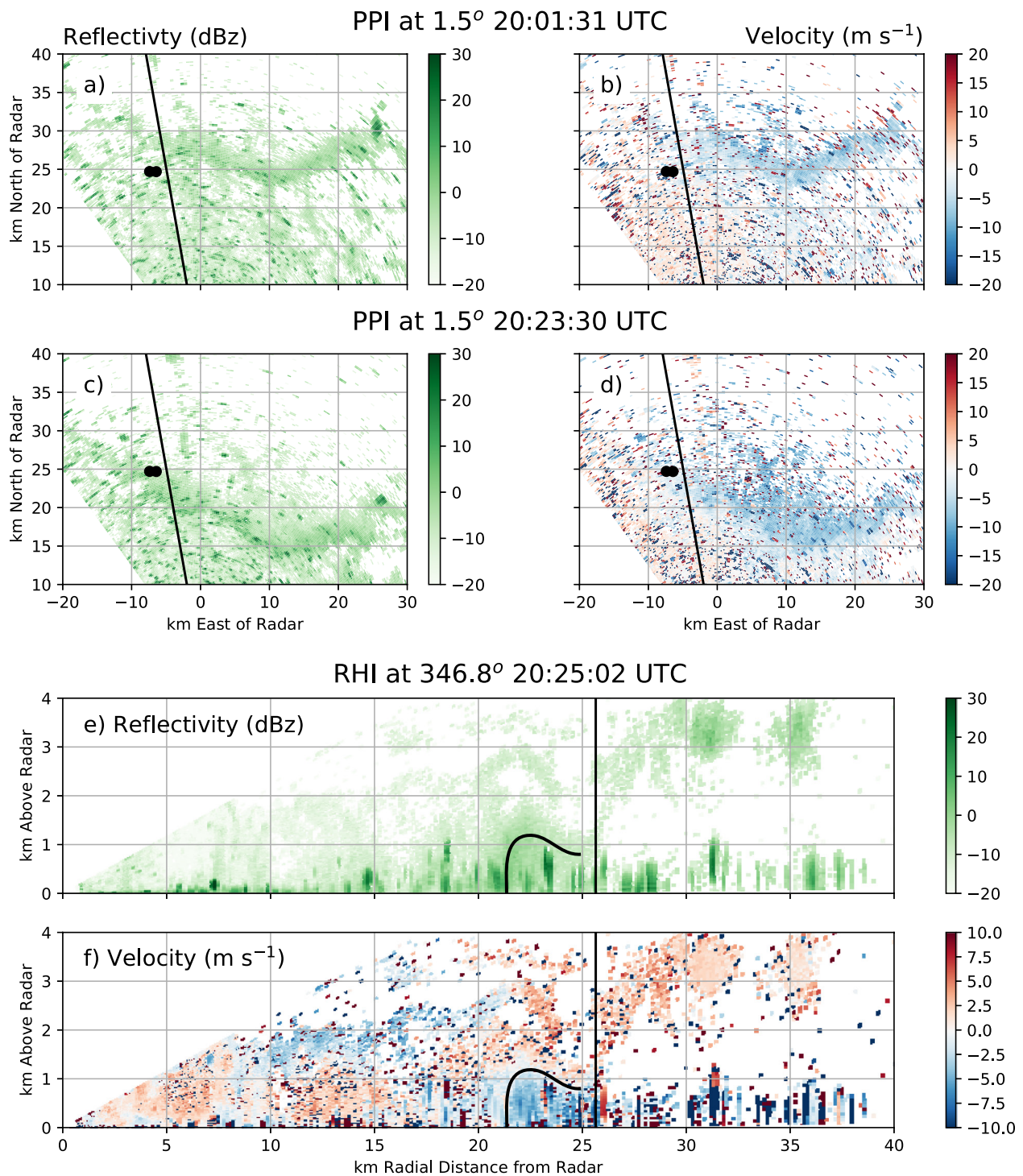


Fig. 10. CSU-CHILL PPI scans at 1.5° elevation angle at two different times corresponding to sounding sets CP1 and CP2, respectively (see text): (a),(c) reflectivity and (b),(d) velocity. The two black dots indicate the ANCHR and 1KM deployment locations of the Flying Curtain, and the black lines show the position of the RHI scan plotted in (e) and (f). RHI scans of (e) reflectivity and (f) velocity at 2025 UTC, with the deployment location indicated by vertical black lines. The solid curved black lines in (e) and (f) represent the approximate location of the outflow boundary of the cold pool. In all panels, data are plotted only where the normalized coherent power is greater than 0.2 in order to eliminate some of the signal noise.

Four pairs of soundings were launched simultaneously from the ANCHR and 1KM points at ~ 20 -min time intervals (Fig. 11). The PRE soundings (1936 UTC, 1336 LT; yellow) were launched before the gust front passage. The CP1 soundings (2001 UTC, 1401 LT; green) were released after a shift in the surface wind direction was observed at the surface stations, while

the CP2 soundings (2023 UTC; 1423 LT; light blue) were launched after the wind speeds had increased and the gust front had passed the Flying Curtain. The release locations of the CP1 and CP2 soundings relative to the position of the gust front are indicated in Figs. 10a–b and 10c–d, respectively. Finally, the CP3 soundings (2042 UTC; 1442 LT; dark blue) were released behind the gust front, well within the propagating cold pool.

During the PRE time period, all the near-surface measurements were relatively steady except for the wind direction (Fig. 12d). Approximately 5–10 min before the CP1 soundings were launched, the surface winds began to shift from being easterly/southeasterly to northeasterly, prompting the decision to release the CP1 soundings. This wind shift was used as an indicator of when to release soundings to sample the gust front for

the remainder of the field campaign. Byers and Braham (1949) also found that the cold pool observations made during the Thunderstorm Project often showed a wind shift well before the temperature dropped, and the radial wind gradient is also located outside of the density potential temperature gradient in the simulation analyses of Drager and van den Heever (2017). The CP1 soundings demonstrate clear thermodynamic differences from the PRE soundings. Both the potential temperature and water vapor mixing ratios are well mixed, with warmer and drier air throughout the lowest 1 km AGL than was observed in the PRE soundings (Figs. 11a,b). At 2023 UTC (1423 LT), the time when the CP2 soundings were launched, the presence of the cold pool started to become evident in the surface and drone observations, including a drop in the temperature (only in the drone data), an increase in the humidity, a continued increase in the wind speed, and the backing of the winds (Fig. 12). The cooling and moistening of the lower 1–1.5 km, as well as the enhanced northeasterly winds, are also evident in the CP2 and CP3 soundings when compared with the PRE and CP1 soundings (Figs. 11a–d).

It is apparent from Figs. 11 and 12 that a time lag exists between the first temperature drop observed by the drones and the soundings, and those observed by the surface stations. The sharpest temperature drop within the drone observations begins between 2017 and 2021 UTC

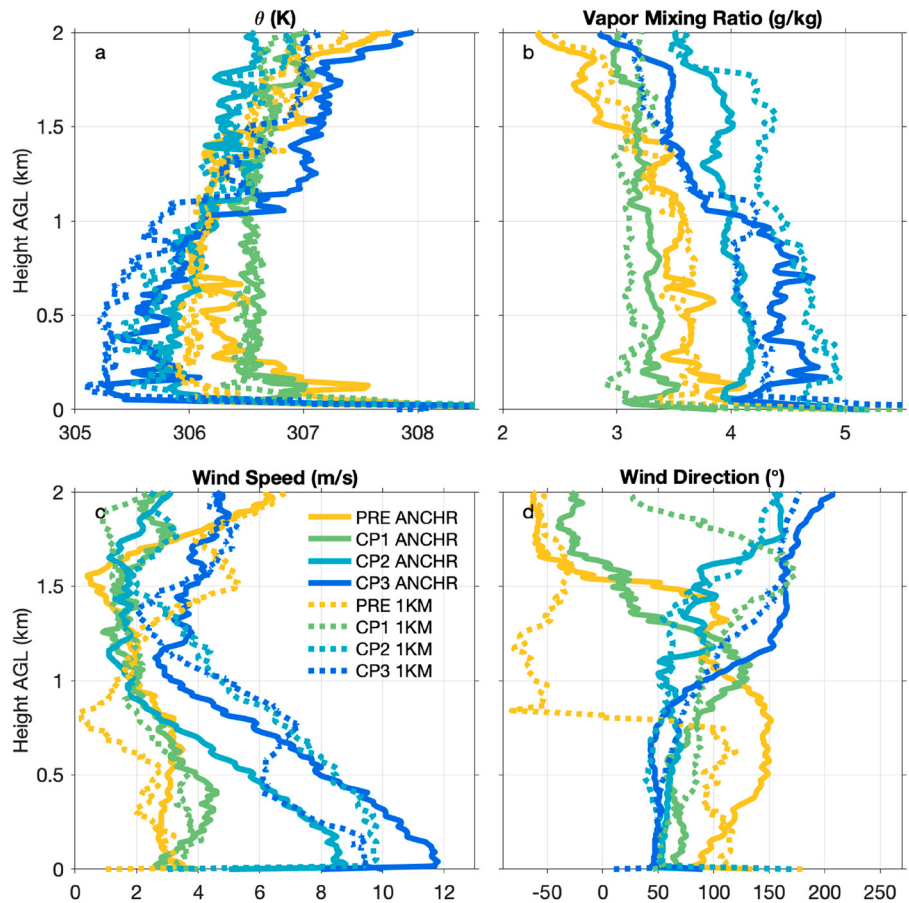


Fig. 11. (a)–(d) Sounding data from the four sets of soundings as indicated in the legend in (c). The PRE soundings (yellow) were released at 1936 UTC (1336 LT) before the cold pool passage; the CP1 soundings (green) at 2001 UTC (1401 LT) after a shift in the surface wind direction; the CP2 soundings (light blue) at 2023 UTC (1423 LT) after the leading edge of the cold pool has passed the instrument wall; and the CP3 soundings (dark blue) at 2042 UTC (1442 LT) behind the gust front. Sounding data are processed by the InterMet software, which includes temporal smoothing and radiation corrections for temperature.

(1417 and 1421 LT), up to 6 min before a similar drop in temperature is observed to begin in the surface station data. The CP2 sounding launched at 2023 UTC (1423 LT) indicates that temperatures above the surface have already decreased, in keeping with the drone observations. The differences between the drone and sounding temperatures from those at the surface stations suggest that different processes are impacting the near surface regions of the cold pool from those further up. While there may be some uncertainty in the exact length of the time period over which the upper- and lower-level temperatures differ given the slower response times of the surface station sensors, the difference is observed over a 6-min time period (which is much longer than the surface station response), which lends confidence to the hypothesis that the processes are indeed different.

These cold pool observations raise several questions about the physical processes critical to cold pool development, propagation, and dissipation. They may be interpreted using the results from a number of recent idealized high-resolution modeling studies. First, the well-mixed and warmer profiles in the CP1 soundings relative to the PRE soundings seem to be counterintuitive given the anticipated drop in temperature with the expected arrival of the cold pool, and that the wind direction had already begun to shift with the passage of the gust front. However, the observed CP1 sounding can potentially be explained by considering what a sounding would look like if it were released just ahead of the simulated

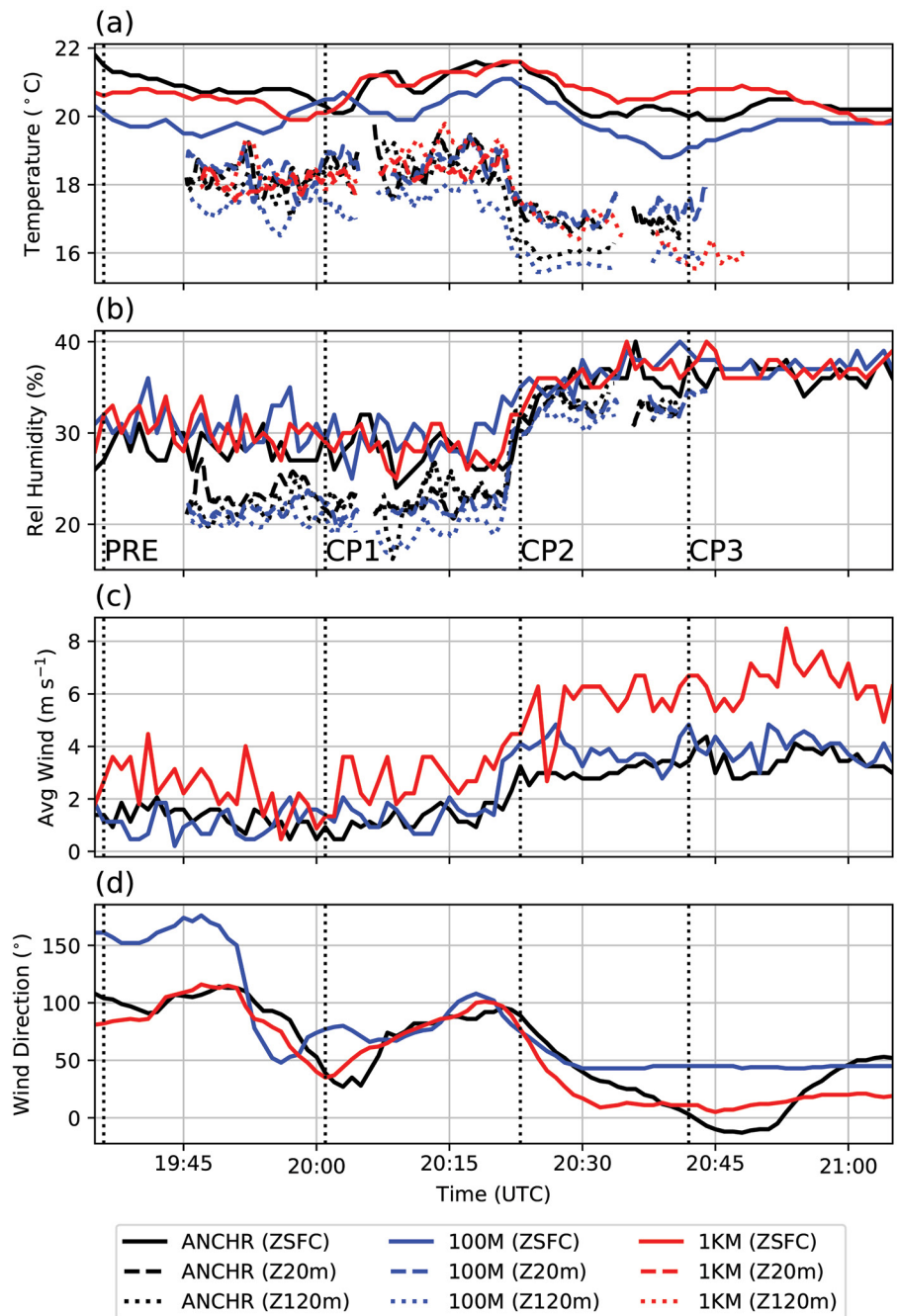


Fig. 12. Time series of near-surface (a) temperature, (b) relative humidity, (c) average wind speed, and (d) wind direction, from the three portable surface stations (solid lines) and stacked pairs of drones (dashed and dotted lines; temperature and relative humidity only) at the three different deployment locations of the Flying Curtain as indicated in the legend. All quantities are 1-min running averages from 1-s data samples. Drone data are shown where the drones are within 10 m of their hovering altitude and where the drone vertical speed is 0.25 m s^{-1} or less. Drone relative humidity data for positions 1KM (Z20m) and 1KM (Z120m) were removed due to data quality issues. Dotted vertical lines indicate the times of the four pairs of sounding launches as labeled in (b).

cold pool of Grant and van den Heever (2016) shown in their Fig. 5c. The simulated cold pool was propagating in a dry convective boundary layer with surface heating, similar to the cold pool observed here. The simulation demonstrates that the near-surface warm environmental air ahead of the cold pool is lifted upward and along the gust front, such that a sounding released just ahead of the cold pool passage would sample this warm, well-mixed air. The observed CP1 water vapor profile is harder to explain. Similar to the potential temperature, the CP1 water vapor is more well mixed than the PRE sounding, but the slight drying trend is not explained solely by vertical mixing within the boundary layer; processes such as lateral advection may be playing a role as well.

Second, the significant time lag between the surface temperature drop observed by the surface stations compared with those evident in the drone observations (Fig. 12) and the CP1 and CP2 soundings (Fig. 11) may be due in part to surface sensible heat fluxes. Grant and van den Heever (2018) demonstrated for a cold pool propagating in a dry convective boundary layer, such as the boundary layer observed here, that the surface sensible heat fluxes are enhanced at the gust front when compared to the surrounding environment. Such a sensible heat flux pattern would warm the near-surface cold pool air more than the cold pool air aloft, thereby potentially resulting in the observed differences in the temporal temperature signals between the surface stations and drones/soundings. The time lag in the temperature drop between the surface stations and drones may also be due in part to surface friction, which slows the progression of the lowest portions of the cold pool in contact with the surface.

Finally, comparisons of the temperature, relative humidity, and wind speed trends at the ANCHR, 100M, and 1KM points reveal the scales over which these variables may vary. Both the surface station data and the drone observations demonstrate temperature differences between the ANCHR point, the 100M point, and the 1KM point on the order of 1–2 K. The surface wind speeds are similar between the ANCHR and 100M points, but are approximately 2 m s^{-1} different from those at the 1KM point. Finally, very little difference is evident in the relative humidity between the ANCHR, 100M, and 1KM points. These results suggest that cold pool temperatures for this case vary on spatial scales of 100 m and 1 km, the surface wind speeds on the order of 1 km, and that relative humidity is relatively consistent over horizontal spatial scales of 100 m and 1 km. These preliminary trends in temperature, humidity and wind speed variability are being investigated for all of the other C³LOUD-Ex cold pools. Should they prove to be robust, they will have significant implications for the vertical and horizontal model grid spacings necessary to resolve cold pool processes.

This case study highlights the strength of using both modeling and observational studies to improve our process-level understanding of cold pools. Additional modeling studies are being conducted of several of the C³LOUD-Ex cold pool cases to further investigate these processes, and to assess how well they are represented in high-resolution LES simulations.

Summary and conclusions

C³LOUD-Ex was conducted to obtain measurements of the spatial and temporal heterogeneities in convective updraft velocities and cold pools with the goal of enhancing our understanding of deep convective storm processes and their representation in numerical models. A number of different instrument platforms including drones, radiosondes, the CSU-CHILL radar, the KCYS and KFTG NEXRAD radars, surface stations, and a disdrometer were simultaneously utilized to obtain independent but synergistic measurements of these storm features. Through the use of a number of novel campaign strategies, including the Flying Curtain and radiosonde-targeted updrafts, extensive measurements of seven supercell updrafts and 16 cold pools were successfully made.

The 16 cold pools observed during C³LOUD-Ex were produced by a range of convective morphologies under a wide variety of conditions. The maximum cold pool temperature

perturbations across all 16 cold pools ranged from -8 K to close to 0 K, the cold pool depths varied from 200 to 2,300 m, and a variety of vertical temperature structures was also evident. An in-depth analysis of the 17 May 2017 cold pool case study demonstrated several interesting results. First, following a wind shift, a warming in the temperature profile was first observed with the passage of the gust front. The warming was followed by a decrease in temperature as the body of the cold pool passed through the Flying Curtain. Similar results have been found in previous high-resolution simulations (Grant and van den Heever 2016) and suggest that this increase in temperature with the passage of the gust front is due to the lifting of the near-surface warm environmental air upward and along the gust front. Second, a significant time lag was found in the drop of the temperature at the surface compared with those at $O(100)$ m above the surface. Based on prior simulations of other similar cold pools (Grant and van den Heever 2018), it is hypothesized that the time lag is likely due to enhanced surface sensible heat fluxes within the gust front and to surface frictional effects. Finally, analysis of the observations collected at the ANCHR, 100M, and 1KM points suggests that cold pool temperatures vary on spatial scales of 100 m and 1 km, while the surface wind speeds vary on the order of 1 km, and the relative humidity appears to be relatively constant over scales of both 100 m and 1 km. However, it should be noted that this finding is for one cold pool case only, and the other C³LOUD-Ex cold pools are being examined to assess the robustness of this finding.

Radiosonde and radar observations of seven supercell storms were successfully obtained. The radiosonde estimates of the maximum supercell updraft velocities throughout the field campaign indicate speeds of 36.2 ± 2.6 m s⁻¹. However, after adjusting for those instances in which there was strong evidence that the radiosonde balloon had burst (Marinescu et al. 2020), the maximum velocity observed was 49.9 m s⁻¹. The observed variability in the updraft velocities is closely linked to the regions of the supercell updraft that were sampled by the radiosonde. These updraft velocity measurements represent a lower bound of the updraft velocity estimates given the uncertainties associated with balloon icing, and that the radiosondes often did not ascend through the middle of the rotating updraft, as determined using collocated radar observations. The fact that these measurements represent a lower bound on the maximum velocities is all the more impressive given that most of the C³LOUD-Ex supercells developed in moderate CAPE environments. Detailed comparisons of the radiosonde and dual-Doppler estimates of the C³LOUD-Ex updraft velocities, where both were available, have been reported by Marinescu et al. (2020). This study shows that the locally high radiosonde estimates that are evident in some of these observations, cannot be captured when using relatively coarse remote sensing methods.

Finally, the analyses of the C³LOUD-Ex observations reported here have several implications for enhancing the numerical modeling of deep convective storms:

- 1) The depth of the C³LOUD-Ex cold pools ranged from 200 to 2300 m. It is therefore important to ensure that vertical grid resolutions are sufficiently high across this depth if we are to accurately represent the range in cold pool depths and processes within numerical weather prediction and research models. Horizontal grid resolutions also need to be carefully considered if the spatial variations in cold pool properties both parallel and perpendicular to the gust front are to be properly simulated. The preliminary analysis conducted here suggests that temperature variability on scales of $O(100)$ m is the most restrictive of the requirements, although additional assessments are needed to determine the robustness of this result. The spatial scale of the observations is in keeping with the suggestions of previous modeling results (Droegemeier and Wilhelmson 1987; Straka et al. 1993; Bryan et al. 2003; Grant and van den Heever 2016).
- 2) The cold pool results shown here clearly demonstrate the strength of using high spatial and temporal resolution datasets, together with high-resolution modeling studies, to

better understand those processes active in the vertical, and along and perpendicular to the gust front. It is in this way that we can better predict the impacts of cold pools on deep convective storms, and hence their intensity, initiation, propagation, and longevity.

- 3) A number of past studies have shown that updraft velocities of simulated deep convective storms may be significantly greater than the corresponding dual-Doppler estimates (Varble et al. 2014; Marinescu et al. 2016; Fan et al. 2017). The C³LOUD-Ex radiosonde estimates of the updraft velocities were at times greater than the dual-Doppler estimates, as demonstrated by Marinescu et al. (2020), which highlights the great strength in using updraft velocity estimates obtained from both radiosondes and radars when evaluating simulated updraft velocities.

Acknowledgments. The insightful and constructive comments from Dr. Jeff Trapp, Dr. Adam Houston, and a third anonymous reviewer are greatly appreciated and resulted in a much clearer manuscript. Funding from the Monfort Excellence Fund provided to Susan C. van den Heever as a Monfort Professor at Colorado State University, as well as funding from the National Science Foundation Grant AGS-1409686 and AGS-2029611 is acknowledged. Peter Marinescu and Sean Freeman were also supported by the National Science Foundation Graduate Research Fellowship Program (Grants DGE-1321845 and DGE-1840343, respectively). We would like to thank the forecasters at the Boulder and Cheyenne NWS Forecast Offices for their insights into our deployment plans and strategies, as well as Mark Benoit from InterMet systems for his assistance with the InterMet radiosonde system and drone instrumentation. Finally, the scientific results and conclusions, as well as any views or opinions expressed herein, are those of the author(s) and do not necessarily reflect those of NOAA or the Department of Commerce.

References

- Benjamin, S. G., and Coauthors, 2016: A North American hourly assimilation and model forecast cycle: The Rapid Refresh. *Mon. Wea. Rev.*, **144**, 1669–1694, <https://doi.org/10.1175/MWR-D-15-0242.1>.
- Benjamin, T. B., 1968: Gravity currents and related phenomena. *J. Fluid Mech.*, **31**, 209–248, <https://doi.org/10.1017/S0022112068000133>.
- Bluestein, H. B., and C. R. Parks, 1983: A synoptic and photographic climatology of low precipitation thunderstorms in the Southern Plains. *Mon. Wea. Rev.*, **111**, 2034–2046, [https://doi.org/10.1175/1520-0493\(1983\)111<2034:ASAPCO>2.0.CO;2](https://doi.org/10.1175/1520-0493(1983)111<2034:ASAPCO>2.0.CO;2).
- , E. W. McCaul, G. P. Byrd, and G. R. Woodall, 1988: Mobile sounding observations of a tornadic storm near the dryline: The Canadian, Texas storm of 7 May 1986. *Mon. Wea. Rev.*, **116**, 1790–1804, [https://doi.org/10.1175/1520-0493\(1988\)116<1790:M500AT>2.0.CO;2](https://doi.org/10.1175/1520-0493(1988)116<1790:M500AT>2.0.CO;2).
- Borque, P., S. W. Nesbitt, R. J. Trapp, S. Lasher-Trapp, and M. Oue, 2020: Observational study of the thermodynamics and morphological characteristics of a midlatitude continental cold pool event. *Mon. Wea. Rev.*, **148**, 719–737, <https://doi.org/10.1175/MWR-D-19-0068.1>.

- Bousquet, O., P. Tabary, and J. Parent du Châtelet, 2008: Operational multiple-Doppler wind retrieval inferred from long-range radial velocity measurements. *J. Appl. Meteor. Climatol.*, **47**, 2929–2945, <https://doi.org/10.1175/2008JAMC1878.1>.
- Brooks, H. E., C. A. Doswell, and R. B. Wilhelmson, 1994: The role of midtropospheric winds in the evolution and maintenance of low-level mesocyclones. *Mon. Wea. Rev.*, **122**, 126–136, [https://doi.org/10.1175/1520-0493\(1994\)122<0126:TROMWI>2.0.CO;2](https://doi.org/10.1175/1520-0493(1994)122<0126:TROMWI>2.0.CO;2).
- Browning, K. A., 1965: The evolution of tornadic storms. *J. Atmos. Sci.*, **22**, 664–668, [https://doi.org/10.1175/1520-0469\(1965\)022<0664:TEOTS>2.0.CO;2](https://doi.org/10.1175/1520-0469(1965)022<0664:TEOTS>2.0.CO;2).
- Brunkow, D., V. N. Bringi, P. C. Kennedy, S. A. Rutledge, V. Chandrasekar, E. A. Mueller, and R. K. Bowie, 2000: A description of the CSU-CHILL national radar facility. *J. Atmos. Oceanic Technol.*, **17**, 1596–1608, [https://doi.org/10.1175/1520-0426\(2000\)017<1596:ADOTCC>2.0.CO;2](https://doi.org/10.1175/1520-0426(2000)017<1596:ADOTCC>2.0.CO;2).
- Bryan, G. H., and M. D. Parker, 2010: Observations of a squall line and its near environment using high-frequency rawinsonde launches during VORTEX2. *Mon. Wea. Rev.*, **138**, 4076–4097, <https://doi.org/10.1175/2010MWR3359.1>.
- , J. C. Wyngaard, and J. M. Fritsch, 2003: Resolution requirements for the simulation of deep moist convection. *Mon. Wea. Rev.*, **131**, 2394–2416, [https://doi.org/10.1175/1520-0493\(2003\)131<2394:RRFTSO>2.0.CO;2](https://doi.org/10.1175/1520-0493(2003)131<2394:RRFTSO>2.0.CO;2).
- , D. Ahijevych, C. Davis, S. Trier, and M. Weisman, 2005: Observations of cold pool properties in mesoscale convective systems during BAMEX. *11th Conf. on Mesoscale Processes*, Albuquerque, NM, Amer. Meteor. Soc., JP5J.12, https://ams.confex.com/ams/32Rad11Meso/techprogram/paper_96718.htm.
- Byers, H. R., and R. R. Braham Jr., 1949: *The Thunderstorm*. U.S. Govt. Printing Office, 287 pp.
- Carbone, R. E., and J. D. Tuttle, 2008: Rainfall occurrence in the U.S. warm season: The diurnal cycle. *J. Climate*, **21**, 4132–4146, <https://doi.org/10.1175/2008JCLI2275.1>.
- Charba, J., 1974: Application of gravity current model to analysis of squall-line gust front. *Mon. Wea. Rev.*, **102**, 140–156, [https://doi.org/10.1175/1520-0493\(1974\)102<0140:AOGCMT>2.0.CO;2](https://doi.org/10.1175/1520-0493(1974)102<0140:AOGCMT>2.0.CO;2).
- Coffer, B. E., M. D. Parker, J. M. L. Dahl, L. J. Wicker, and A. J. Clark, 2017: Volatility of tornadogenesis: An example of simulated nontorandic and tornadic supercells in VORTEX2 environments. *Mon. Wea. Rev.*, **145**, 4605–4625, <https://doi.org/10.1175/MWR-D-17-0152.1>.
- Collis, S., A. Protat, and K.-S. Chung, 2010: The effect of radial velocity gridding artifacts on variationally retrieved vertical velocities. *J. Atmos. Oceanic Technol.*, **27**, 1239–1246, <https://doi.org/10.1175/2010JTECHA1402.1>.
- Cotton, W. R., G. H. Bryan, and S. C. van den Heever, 2010: *Storm and Cloud Dynamics*. 2nd ed. Academic Press, 820 pp.
- Davies-Jones, R. P., and J. H. Henderson, 1975: Updraft properties deduced statistically from Rawin soundings. *Pure Appl. Geophys.*, **113**, 787–801, <https://doi.org/10.1007/BF01592959>.
- , D. W. Burgess, and L. R. Lemon, 1976: An atypical tornado-producing cumulonimbus. *Weather*, **31**, 337–347, <https://doi.org/10.1002/j.1477-8696.1976.tb07449.x>.
- Davis, C., and Coauthors, 2004: The Bow Echo and MCV Experiment: Observations and opportunities. *Bull. Amer. Meteor. Soc.*, **85**, 1075–1094, <https://doi.org/10.1175/BAMS-85-8-1075>.
- Davis Instruments, 2013: Wireless Vantage Pro2 ISS with 24-Hr fan aspirated radiation shield specifications. Accessed 20 June 2019, www.davisinstruments.com/product/wireless-vantage-pro2-iss-with-24-hr-fan-aspirated-radiation-shield/.
- Dawson, D. T., M. Xue, J. A. Milbrandt, and M. K. Yau, 2010: Comparison of evaporation and cold pool development between single-moment and multimoment bulk microphysics schemes in idealized simulations of tornadic thunderstorms. *Mon. Wea. Rev.*, **138**, 1152–1171, <https://doi.org/10.1175/2009MWR2956.1>.
- DiGangi, E. A., D. R. MacGorman, C. L. Ziegler, D. Betten, M. Biggerstaff, M. Bowlan, and C. K. Potvin, 2016: An overview of the 29 May 2012 Kingfisher supercell during DC3. *J. Geophys. Res. Atmos.*, **121**, 14316–14343, <https://doi.org/10.1002/2016JD025690>.
- DJI, 2016: Matrice 600 specifications. Accessed 21 May 2019, www.dji.com/matrice600/info#specs.
- DJI, 2017: Matrice 600 pro specifications. Accessed 21 May 2019, www.dji.com/matrice600-pro/info#specs.
- Doswell, C. A., III, 2001: Severe convective storms—An overview. *Severe Convective Storms, Meteor. Monogr.*, No. 50, Amer. Meteor. Soc., 1–26, <https://doi.org/10.1175/0065-9401-28.50.1>.
- , and D. W. Burgess, 1993: Tornadoes and tornadic storms: A review of conceptual models. *The Tornado: Its Structure, Dynamics, Prediction, and Hazards*, Geophys. Monogr., Vol. 79, Amer. Geophys. Union, 161–172.
- Drager, A. J., and S. C. van den Heever, 2017: Characterizing convective cold pools. *J. Adv. Model. Earth Syst.*, **9**, 1091–1115, <https://doi.org/10.1002/2016MS000788>.
- , L. D. Grant, and S. C. van den Heever, 2020: Cold pool responses to changes in soil moisture. *J. Adv. Model. Earth Syst.*, **12**, e2019MS001922, <https://doi.org/10.1029/2019MS001922>.
- Dröegemeier, K. K., and R. B. Wilhelmson, 1985: Three-dimensional numerical modeling of convection produced by interacting thunderstorm outflows. Part I: Control simulation and low-level moisture variations. *J. Atmos. Sci.*, **42**, 2381–2403, [https://doi.org/10.1175/1520-0469\(1985\)042<2381:TDNOC>2.0.CO;2](https://doi.org/10.1175/1520-0469(1985)042<2381:TDNOC>2.0.CO;2).
- , and ———, 1987: Numerical simulation of thunderstorm outflow dynamics. Part I: Outflow sensitivity experiments and turbulence dynamics. *J. Atmos. Sci.*, **44**, 1180–1210, [https://doi.org/10.1175/1520-0469\(1987\)044<1180:NSOTOD>2.0.CO;2](https://doi.org/10.1175/1520-0469(1987)044<1180:NSOTOD>2.0.CO;2).
- Eastin, M. D., T. L. Gardner, M. C. Link, and K. C. Smith, 2012: Surface cold pools in the outer rainbands of Tropical Storm Hanna (2008) near landfall. *Mon. Wea. Rev.*, **140**, 471–491, <https://doi.org/10.1175/MWR-D-11-00099.1>.
- Engerer, N. A., D. J. Stensrud, and M. C. Coniglio, 2008: Surface characteristics of observed cold pools. *Mon. Wea. Rev.*, **136**, 4839–4849, <https://doi.org/10.1175/2008MWR2528.1>.
- Fan, J., and Coauthors, 2017: Cloud-resolving model intercomparison of an MC3E squall line case: Part I—Convective updrafts. *J. Geophys. Res. Atmos.*, **122**, 9351–9378, <https://doi.org/10.1002/2017JD026622>.
- Fast, J. D., L. K. Berg, Z. Feng, F. Mei, R. Newsom, K. Sakaguchi, and H. Xiao, 2019: The impact of variable land-atmosphere coupling on convective cloud populations observed during the 2016 HI-SCALE field campaign. *J. Adv. Model. Earth Syst.*, **11**, 2629–2654, <https://doi.org/10.1029/2019MS001727>.
- Federal Aviation Administration, 2017: Part 107 Waivers Granted. Accessed 28 June 2017, https://web.archive.org/web/20170628182836/https://www.faa.gov/uas/request_waiver/waivers_granted/.
- Feng, Z., S. Hagos, A. K. Rowe, C. D. Burleyson, M. N. Martini, and S. P. de Szoeke, 2015: Mechanisms of convective cloud organization by cold pools over tropical warm ocean during the AMIE/DYNAMO field campaign. *J. Adv. Model. Earth Syst.*, **7**, 357–381, <https://doi.org/10.1002/2014MS000384>.
- Friedrich, K., S. Higgins, F. J. Masters, and C. R. Lopez, 2013: Articulating and stationary Parsivel disdrometer measurements in conditions with strong winds and heavy rainfall. *J. Atmos. Oceanic Technol.*, **30**, 2063–2080, <https://doi.org/10.1175/JTECH-D-12-00254.1>.
- Gaynor, J. E., and P. A. Mandics, 1978: Analysis of the tropical marine boundary layer during GATE using acoustic sounder data. *Mon. Wea. Rev.*, **106**, 223–232, [https://doi.org/10.1175/1520-0493\(1978\)106<0223:AOTTMB>2.0.CO;2](https://doi.org/10.1175/1520-0493(1978)106<0223:AOTTMB>2.0.CO;2).
- Geerts, B., and Coauthors, 2017: The 2015 Plains Elevated Convection at Night field project. *Bull. Amer. Meteor. Soc.*, **98**, 767–786, <https://doi.org/10.1175/BAMS-D-15-00257.1>.
- Gentine, P., A. Garelli, S. Park, J. Nie, G. Torri, and Z. Kuang, 2016: Role of surface heat fluxes underneath cold pools. *Geophys. Res. Lett.*, **43**, 874–883, <https://doi.org/10.1002/2015GL067262>.
- Goff, R. C., 1976: Vertical structure of thunderstorm outflows. *Mon. Wea. Rev.*, **104**, 1429–1440, [https://doi.org/10.1175/1520-0493\(1976\)104<1429:VSOTO>2.0.CO;2](https://doi.org/10.1175/1520-0493(1976)104<1429:VSOTO>2.0.CO;2).
- Grant, L. D., and S. C. van den Heever, 2014: Microphysical and dynamical characteristics of low-precipitation and classic supercells. *J. Atmos. Sci.*, **71**, 2604–2624, <https://doi.org/10.1175/JAS-D-13-0261.1>.
- , and ———, 2015: Cold pool and precipitation responses to aerosol loading: Modulation by dry layers. *J. Atmos. Sci.*, **72**, 1398–1408, <https://doi.org/10.1175/JAS-D-14-0260.1>.

- , and —, 2016: Cold pool dissipation. *J. Geophys. Res. Atmos.*, **121**, 1138–1155, <https://doi.org/10.1002/2015JD023813>.
- , and —, 2018: Cold pool-land surface interactions in a dry continental environment. *J. Adv. Model. Earth Syst.*, **10**, 1513–1526, <https://doi.org/10.1029/2018MS001323>.
- , M. W. Moncrieff, T. P. Lane, and S. C. van den Heever, 2020: Shear-parallel tropical convective systems: Importance of cold pools and wind shear. *Geophys. Res. Lett.*, **47**, 503, <https://doi.org/10.1029/2020GL087720>.
- Greene, B. R., A. R. Segales, T. M. Bell, E. A. Pillar-Little, and P. B. Chilson, 2019: Environmental and sensor integration influences on temperature measurements by rotary-wing unmanned aircraft systems. *Sensors*, **19**, 1470, <https://doi.org/10.3390/s19061470>.
- Hartmann, D. L., 2016: Tropical anvil clouds and climate sensitivity. *Proc. Natl. Acad. Sci. USA*, **113**, 8897–8899, <https://doi.org/10.1073/pnas.1610455113>.
- Herman, G. R., E. R. Nielsen, and R. S. Schumacher, 2018: Probabilistic verification of storm prediction center convective outlooks. *Wea. Forecasting*, **33**, 161–184, <https://doi.org/10.1175/WAF-D-17-0104.1>.
- Hirt, M., G. C. Craig, S. A. K. Schäfer, J. Savre, and R. Heinze, 2020: Cold pool driven convective initiation: Using causal graph analysis to determine what convection permitting models are missing. *Quart. J. Roy. Meteor. Soc.*, **146**, 2205–2227, <https://doi.org/10.1002/qj.3788>.
- Hitchcock, S. M., R. S. Schumacher, and G. R. Herman, 2019: Evolution of pre- and postconvective environmental profiles from mesoscale convective systems during PECAN. *Mon. Wea. Rev.*, **147**, 2329–2354, <https://doi.org/10.1175/MWR-D-18-0231.1>.
- Houston, A. L., 2016: The sensitivity of deep ascent of cold pool air to vertical shear and cold pool buoyancy. *Electron. J. Severe Storms Meteor.*, **11** (3), www.ejssm.org/ojs/index.php/ejssm/article/viewArticle/151.
- , and R. B. Wilhelmson, 2011: The dependence of storm longevity on the pattern of deep convection initiation in a low-shear environment. *Mon. Wea. Rev.*, **139**, 3125–3138, <https://doi.org/10.1175/MWR-D-10-05036.1>.
- , B. Argrow, J. Elston, J. Lahowetz, E. W. Frew, and P. C. Kennedy, 2012: The Collaborative Colorado–Nebraska Unmanned Aircraft System Experiment. *Bull. Amer. Meteor. Soc.*, **93**, 39–54, <https://doi.org/10.1175/2011BAMS3073.1>.
- International Met Systems, 2016: iMet-XQ data sheet. Accessed 25 May 2019, www.intermetsystems.com/ee/pdf/202020_iMet-XQ_161005.pdf.
- Islam, A., A. L. Houston, A. Shankar, and C. Detweiler, 2019: Design and evaluation of sensor housing for boundary layer profiling using multirotors. *Sensors*, **19**, 2481, <https://doi.org/10.3390/s19112481>.
- Jeevanjee, N., 2017: Vertical velocity in the gray zone. *J. Adv. Model. Earth Syst.*, **9**, 2304–2316, <https://doi.org/10.1002/2017MS001059>.
- , and D. M. Romps, 2013: Convective self-aggregation, cold pools, and domain size. *Geophys. Res. Lett.*, **40**, 994–998, <https://doi.org/10.1002/grl.50204>.
- Jensen, M. P., and Coauthors, 2016: The Midlatitude Continental Convective Clouds Experiment (MC3E). *Bull. Amer. Meteor. Soc.*, **97**, 1667–1686, <https://doi.org/10.1175/BAMS-D-14-00228.1>.
- Johnson, R. H., and P. J. Hamilton, 1988: The relationship of surface pressure features to the precipitation and airflow structure of an intense midlatitude squall line. *Mon. Wea. Rev.*, **116**, 1444–1473, [https://doi.org/10.1175/1520-0493\(1988\)116<1444:TROSPF>2.0.CO;2](https://doi.org/10.1175/1520-0493(1988)116<1444:TROSPF>2.0.CO;2).
- Junyent, F., V. Chandrasekar, V. N. Bringi, S. A. Rutledge, P. C. Kennedy, D. Brunkow, J. George, and R. Bowie, 2015: Transformation of the CSU-CHILL radar facility to a dual frequency, dual-polarization, Doppler system. *Bull. Amer. Meteor. Soc.*, **96**, 975–996, <https://doi.org/10.1175/BAMS-D-13-00150.1>.
- Lebo, Z. J., and H. Morrison, 2015: Effects of horizontal and vertical grid spacing on mixing in simulated squall lines and implications for convective strength and structure. *Mon. Wea. Rev.*, **143**, 4355–4375, <https://doi.org/10.1175/MWR-D-15-0154.1>.
- Lehmiller, G. S., H. B. Bluestein, P. J. Neiman, F. M. Ralph, and W. F. Feltz, 2001: Wind structure in a supercell thunderstorm as measured by a UHF wind profiler. *Mon. Wea. Rev.*, **129**, 1968–1986, [https://doi.org/10.1175/1520-0493\(2001\)129<1968:WSIAST>2.0.CO;2](https://doi.org/10.1175/1520-0493(2001)129<1968:WSIAST>2.0.CO;2).
- LeMone, M. A., and E. J. Zipser, 1980: Cumulonimbus vertical velocity events in GATE. Part I: Diameter, intensity and mass flux. *J. Atmos. Sci.*, **37**, 2444–2457, [https://doi.org/10.1175/1520-0469\(1980\)037<2444:CVVEIG>2.0.CO;2](https://doi.org/10.1175/1520-0469(1980)037<2444:CVVEIG>2.0.CO;2).
- Lindsey, D. T., L. Grasso, J. F. Dostalek, and J. Kerkmann, 2014: Use of the GOES-R split-window difference to diagnose deepening low-level water vapor. *J. Appl. Meteor. Climatol.*, **53**, 2005–2016, <https://doi.org/10.1111+75/JAMC-D-14-0010.1>.
- , D. Bikos, and L. Grasso, 2018: Using the GOES-16 split window difference to detect a boundary prior to cloud formation. *Bull. Amer. Meteor. Soc.*, **99**, 1541–1544, <https://doi.org/10.1175/BAMS-D-17-0141.1>.
- Liu, C., and M. W. Moncrieff, 2000: Simulated density currents in idealized stratified environments. *Mon. Wea. Rev.*, **128**, 1420–1437, [https://doi.org/10.1175/1520-0493\(2000\)128<1420:SDCHIS>2.0.CO;2](https://doi.org/10.1175/1520-0493(2000)128<1420:SDCHIS>2.0.CO;2).
- Lock, N. A., and A. L. Houston, 2015: Spatiotemporal distribution of thunderstorm initiation in the US Great Plains from 2005 to 2007. *Int. J. Climatol.*, **35**, 4047–4056, <https://doi.org/10.1002/joc.4261>.
- Marinescu, P. J., S. C. van den Heever, S. M. Saleeby, and S. M. Kreidenweis, 2016: The microphysical contributions to and evolution of latent heating profiles in two MC3E MCs. *J. Geol. Res.*, **121**, 7913–7935, <https://doi.org/10.1002/2016JD024762>.
- , P. C. Kennedy, M. M. Bell, A. J. Drager, L. D. Grant, S. W. Freeman, and S. C. van den Heever, 2020: Updraft vertical velocity observations and uncertainties in High Plains supercells using radiosondes and radars. *Mon. Wea. Rev.*, **148**, 4435–4452, <https://doi.org/10.1175/MWR-D-20-0071.1>.
- Marion, G. R., and R. J. Trapp, 2019: The dynamical coupling of convective updrafts, downdrafts, and cold pools in simulated supercell thunderstorms. *J. Geophys. Res. Atmos.*, **124**, 664–683, <https://doi.org/10.1029/2018JD029055>.
- Markowski, P. M., and Y. P. Richardson, 2009: Tornadogenesis: Our current understanding, forecasting considerations, and questions to guide future research. *Atmos. Res.*, **93**, 3–10, <https://doi.org/10.1016/j.atmosres.2008.09.015>.
- , J. M. Straka, and E. N. Rasmussen, 2002: Direct surface thermodynamic observations within the rear-flank downdrafts of nontornadic and tornadic supercells. *Mon. Wea. Rev.*, **130**, 1692–1721, [https://doi.org/10.1175/1520-0493\(2002\)130<1692:DSTOWT>2.0.CO;2](https://doi.org/10.1175/1520-0493(2002)130<1692:DSTOWT>2.0.CO;2).
- McCaul, E. W., Jr., and C. Cohen, 2002: The impact on simulated storm structure and intensity of variations in the mixed layer and moist layer depths. *Mon. Wea. Rev.*, **130**, 1722–1748, [https://doi.org/10.1175/1520-0493\(2002\)130<1722:TIOSSS>2.0.CO;2](https://doi.org/10.1175/1520-0493(2002)130<1722:TIOSSS>2.0.CO;2).
- Miller, L. J., and S. M. Fredrick, 1998: Custom Editing and Display of Reduced Information in Cartesian space (CEDRIC) manual. National Center for Atmospheric Research, Mesoscale and Microscale Meteorology Division, 130 pp.
- Morrison, H., S. A. Tessendorf, K. Ikeda, and G. Thompson, 2012: Sensitivity of a simulated midlatitude squall line to parameterization of raindrop breakup. *Mon. Wea. Rev.*, **140**, 2437–2460, <https://doi.org/10.1175/MWR-D-11-00283.1>.
- Mullendore, G. L., D. R. Durran, and J. R. Holton, 2005: Cross-tropopause tracer transport in midlatitude convection. *J. Geophys. Res.*, **110**, D06113, <https://doi.org/10.1029/2004JD005059>.
- Musil, D. J., A. J. Heymsfield, and P. L. Smith, 1986: Microphysical characteristics of a well-developed weak echo region in a high plains supercell thunderstorm. *J. Climate Appl. Meteor.*, **25**, 1037–1051, [https://doi.org/10.1175/1520-0450\(1986\)025<1037:MCOAWD>2.0.CO;2](https://doi.org/10.1175/1520-0450(1986)025<1037:MCOAWD>2.0.CO;2).
- NASEM, 2018: *Thriving on Our Changing Planet: A Decadal Strategy for Earth Observation from Space*. The National Academies Press, 716 pp., <https://doi.org/10.17226/24938>.
- Nelson, S. P., and R. A. Brown, 1987: Error sources and accuracy of vertical velocities computed from multiple-Doppler radar measurements in deep convective storms. *J. Atmos. Oceanic Technol.*, **4**, 233–238, [https://doi.org/10.1175/1520-0426\(1987\)004<0233:ESAAOV>2.0.CO;2](https://doi.org/10.1175/1520-0426(1987)004<0233:ESAAOV>2.0.CO;2).
- Nesbitt, S. W., R. Cifelli, and S. A. Rutledge, 2006: Storm morphology and rainfall characteristics of TRMM precipitation features. *Mon. Wea. Rev.*, **134**, 2702–2721, <https://doi.org/10.1175/MWR3200.1>.
- NOAA, 1991: NOAA Next Generation Radar (NEXRAD) Level 2 Base Data. NOAA National Centers for Environmental Information, accessed 14 May 2019, <https://doi.org/10.7289/V5W9574V>.

- Oue, M., P. Kollias, A. Shapiro, A. Tatarevic, and T. Matsui, 2019: Investigation of observational error sources in multi-Doppler-radar three-dimensional variational vertical air motion retrievals. *Atmos. Meas. Tech.*, **12**, 1999–2018, <https://doi.org/10.5194/amt-12-1999-2019>.
- Potvin, C. K., L. J. Wicker, and A. Shapiro, 2012: Assessing errors in variational dual-Doppler wind syntheses of supercell thunderstorms observed by storm-scale mobile radars. *J. Atmos. Oceanic Technol.*, **29**, 1009–1025, <https://doi.org/10.1175/JTECH-D-11-00177.1>.
- Purdum, J. F. W., 1976: Some uses of high-resolution GOES imagery in the mesoscale forecasting of convection and its behavior. *Mon. Wea. Rev.*, **104**, 1474–1483, [https://doi.org/10.1175/1520-0493\(1976\)104<1474:SUOHRG>2.0.CO;2](https://doi.org/10.1175/1520-0493(1976)104<1474:SUOHRG>2.0.CO;2).
- , 1982: Subjective interpretation of geostationary satellite data for nowcasting. *Nowcasting*, K. Browning, Ed., Academic Press, 149–166.
- Rasmussen, E. N., J. M. Straka, R. Davies-Jones, C. A. Doswell, F. H. Carr, M. D. Eilts, and D. R. MacGorman, 1994: Verification of the Origins of Rotation in Tornadoes Experiment: VORTEX. *Bull. Amer. Meteor. Soc.*, **75**, 995–1006, [https://doi.org/10.1175/1520-0477\(1994\)075<0995:VOTOOR>2.0.CO;2](https://doi.org/10.1175/1520-0477(1994)075<0995:VOTOOR>2.0.CO;2).
- Riehl, H., and J. S. Malkus, 1958: On the heat balance in the equatorial trough zone. *Geophysica*, **6**, 503–538.
- Riganti, C. J., and A. L. Houston, 2017: Rear-flank outflow dynamics and thermodynamics in the 10 June 2010 Last Chance, Colorado, supercell. *Mon. Wea. Rev.*, **145**, 2487–2504, <https://doi.org/10.1175/MWR-D-16-0128.1>.
- Rotunno, R., J. B. Klemp, and M. L. Weisman, 1988: A theory for strong, long-lived squall lines. *J. Atmos. Sci.*, **45**, 463–485, [https://doi.org/10.1175/1520-0469\(1988\)045<0463:ATFSL>2.0.CO;2](https://doi.org/10.1175/1520-0469(1988)045<0463:ATFSL>2.0.CO;2).
- Schwartz, C. S., G. S. Romine, R. A. Sobash, K. R. Fossell, and M. L. Weisman, 2015: NCAR's experimental real-time convection-allowing ensemble prediction system. *Wea. Forecasting*, **30**, 1645–1654, <https://doi.org/10.1175/WAF-D-15-0103.1>.
- Seigel, R. B., and S. C. van den Heever, 2012: Simulated density currents beneath embedded stratified layers. *J. Atmos. Sci.*, **69**, 2192–2200, <https://doi.org/10.1175/JAS-D-11-0255.1>.
- Simpson, J., N. Westcott, R. Clerman, and R. A. Pielke, 1980: On cumulus mergers. *Arch. Meteor. Geophys. Bioklimatol.*, **29A**, 1–40.
- Snook, N., and M. Xue, 2008: Effects of microphysical drop size distribution on tornadogenesis in supercell thunderstorms. *Geophys. Res. Lett.*, **35**, L24803, <https://doi.org/10.1029/2008GL035866>.
- Soderholm, J., H. McGowan, H. Richter, K. Walsh, T. Weckwerth, and M. Coleman, 2016: The Coastal Convective Interactions Experiment (CCIE): Understanding the role of sea breezes for hailstorm hotspots in eastern Australia. *Bull. Amer. Meteor. Soc.*, **97**, 1687–1698, <https://doi.org/10.1175/BAMS-D-14-00212.1>.
- Straka, J. M., R. B. Wilhelmson, L. J. Wicker, J. R. Anderson, and K. K. Droegemeier, 1993: Numerical solutions of a non-linear density current: A benchmark solution and comparisons. *Int. J. Numer. Methods Fluids*, **17**, 1–22, <https://doi.org/10.1002/flid.1650170103>.
- Szoke, E. J., 1991: Eye of the Denver cyclone. *Mon. Wea. Rev.*, **119**, 1283–1292, [https://doi.org/10.1175/1520-0493\(1991\)119<1283:EOTDC>2.0.CO;2](https://doi.org/10.1175/1520-0493(1991)119<1283:EOTDC>2.0.CO;2).
- Thorpe, A. J., M. J. Miller, and M. W. Moncrieff, 1982: Two-dimensional convection in non-constant shear: A model of mid-latitude squall lines. *Quart. J. Roy. Meteor. Soc.*, **108**, 739–762, <https://doi.org/10.1002/qj.49710845802>.
- Tompkins, A. M., 2001: Organization of tropical convection in low vertical wind shears: The role of cold pools. *J. Atmos. Sci.*, **58**, 1650–1672, [https://doi.org/10.1175/1520-0469\(2001\)058<1650:OOTCIL>2.0.CO;2](https://doi.org/10.1175/1520-0469(2001)058<1650:OOTCIL>2.0.CO;2).
- Toth, J. J., and R. H. Johnson, 1985: Summer surface flow characteristics over northeast Colorado. *Mon. Wea. Rev.*, **113**, 1458–1469, [https://doi.org/10.1175/1520-0493\(1985\)113<1458:SSFCO>2.0.CO;2](https://doi.org/10.1175/1520-0493(1985)113<1458:SSFCO>2.0.CO;2).
- Trapp, R. J., D. J. Stensrud, M. C. Coniglio, R. S. Schumacher, M. E. Baldwin, S. Waugh, and D. T. Conlee, 2016: Mobile radiosonde deployments during the Mesoscale Predictability Experiment (MPEX): Rapid and adaptive sampling of upscale convective feedbacks. *Bull. Amer. Meteor. Soc.*, **97**, 329–336, <https://doi.org/10.1175/BAMS-D-14-00258.1>.
- van den Heever, S. C., and W. R. Cotton, 2004: The impact of hail size on simulated supercell storms. *J. Atmos. Sci.*, **61**, 1596–1609, [https://doi.org/10.1175/1520-0469\(2004\)061<1596:TIOHSO>2.0.CO;2](https://doi.org/10.1175/1520-0469(2004)061<1596:TIOHSO>2.0.CO;2).
- Varble, A., and Coauthors, 2014: Evaluation of cloud-resolving and limited area model intercomparison simulations using TWP-ICE observations: 1. Deep convective updraft properties. *J. Geophys. Res. Atmos.*, **119**, 13 891–13 918, <https://doi.org/10.1002/2013JD021371>.
- Wakimoto, R. M., 1982: The life cycle of thunderstorm gust fronts as viewed with Doppler radar and rawinsonde data. *Mon. Wea. Rev.*, **110**, 1060–1082, [https://doi.org/10.1175/1520-0493\(1982\)110<1060:TLCOTG>2.0.CO;2](https://doi.org/10.1175/1520-0493(1982)110<1060:TLCOTG>2.0.CO;2).
- Wang, J., J. Bian, W. O. Brown, H. Cole, V. Grubišić, and K. Young, 2009: Vertical air motion from T-REX radiosonde and dropsonde data. *J. Atmos. Oceanic Technol.*, **26**, 928–942, <https://doi.org/10.1175/2008JTECHA1240.1>.
- Weckwerth, T. M., and R. M. Wakimoto, 1992: The initiation and organization of convective cells atop a cold-air outflow boundary. *Mon. Wea. Rev.*, **120**, 2169–2187, [https://doi.org/10.1175/1520-0493\(1992\)120<2169:TIAOC>2.0.CO;2](https://doi.org/10.1175/1520-0493(1992)120<2169:TIAOC>2.0.CO;2).
- , H. V. Murphey, C. Flamant, J. Goldstein, and C. R. Pettet, 2008: An observational study of convection initiation on 12 June 2002 during IHOP_2002. *Mon. Wea. Rev.*, **136**, 2283–2304, <https://doi.org/10.1175/2007MWR2128.1>.
- Weisman, M. L., and J. B. Klemp, 1982: The dependence of numerically simulated convective storms on vertical wind shear and buoyancy. *Mon. Wea. Rev.*, **110**, 504–520, [https://doi.org/10.1175/1520-0493\(1982\)110<0504:TDonSC>2.0.CO;2](https://doi.org/10.1175/1520-0493(1982)110<0504:TDonSC>2.0.CO;2).
- , and Coauthors, 2015: The Mesoscale Predictability Experiment (MPEX). *Bull. Amer. Meteor. Soc.*, **96**, 2127–2149, <https://doi.org/10.1175/BAMS-D-13-00281.1>.
- Wilhelmson, R. B., and C.-S. Chen, 1982: A simulation of the development of successive cells along a cold outflow boundary. *J. Atmos. Sci.*, **39**, 1466–1483, [https://doi.org/10.1175/1520-0469\(1982\)039<1466:ASOTDO>2.0.CO;2](https://doi.org/10.1175/1520-0469(1982)039<1466:ASOTDO>2.0.CO;2).
- Wilson, J. W., and C. K. Mueller, 1993: Nowcasts of thunderstorm initiation and evolution. *Wea. Forecasting*, **8**, 113–131, [https://doi.org/10.1175/1520-0434\(1993\)008<0113:NOTIAE>2.0.CO;2](https://doi.org/10.1175/1520-0434(1993)008<0113:NOTIAE>2.0.CO;2).
- Wurman, J., D. Dowell, Y. Richardson, P. Markowski, E. Rasmussen, D. Burgess, L. Wicker, and H. B. Bluestein, 2012: The second verification of the origins of rotation in tornadoes experiment: VORTEX2. *Bull. Amer. Meteor. Soc.*, **93**, 1147–1170, <https://doi.org/10.1175/BAMS-D-11-00010.1>.
- Xue, M., Q. Xu, and K. K. Droegemeier, 1997: A theoretical and numerical study of density currents in non-constant shear flows. *J. Atmos. Sci.*, **54**, 1998–2019, [https://doi.org/10.1175/1520-0469\(1997\)054<1998:ATANSO>2.0.CO;2](https://doi.org/10.1175/1520-0469(1997)054<1998:ATANSO>2.0.CO;2).
- Zhang, X., G. C. Hegerl, S. I. Seneviratne, R. Stewart, F. W. Zwiers, and L. V. Alexander, 2013: WCRP Grand Challenge: Understanding and predicting weather and climate extremes. White Paper, 10 pp., www.wcrp-climate.org/gc-extremes-documents.
- Zipser, E. J., and M. A. Lemone, 1980: Cumulonimbus vertical velocity events in GATE. Part II: Synthesis and model core structure. *J. Atmos. Sci.*, **37**, 2458–2469, [https://doi.org/10.1175/1520-0469\(1980\)037<2458:CVVEIG>2.0.CO;2](https://doi.org/10.1175/1520-0469(1980)037<2458:CVVEIG>2.0.CO;2).
- , C. Liu, D. J. Cecil, S. W. Nesbitt, and D. P. Yorty, 2006: Where are the most intense thunderstorms on Earth? *Bull. Amer. Meteor. Soc.*, **87**, 1057–1072, <https://doi.org/10.1175/BAMS-87-8-1057>.
- Zuidema, P., G. Torri, C. Muller, and A. Chandra, 2017: A Survey of precipitation-induced atmospheric cold pools over oceans and their interactions with the larger-scale environment. *Surv. Geophys.*, **38**, 1283–1305, <https://doi.org/10.1007/s10712-017-9447-x>.